geotechnics

MDPI

Article

Effect of Relative Density on Liquefaction Resistance of Sand Under Simulated Earthquake Loading

Sawash Mohammed * and Hadi Bahadori

Department of Civil Engineering, Faculty of Engineering, Urmia University, Urmia 5756151818, Iran; h.bahadori@urmia.ac.ir

* Correspondence: sawash.m.mohammed@gmail.com

Abstract

Soil liquefaction threatens structures in seismic zones, reducing bearing capacity and causing damage. This research examines how relative density affects Firuzkuh sand's liquefaction resistance under conditions that replicate the 1999 Kocaeli earthquake. Soil samples with relative densities of 0.30 (loose), 0.40 (medium-dense), and 0.50 (medium-dense) underwent 1-g shaking table tests with scaled building models. Cement-stabilized sand columns arranged in a triangular configuration were employed for ground enhancement. Measurements of acceleration, pore-water pressure, and settlement were conducted. Results indicate that increased relative density markedly enhances liquefaction resistance. The peak pore pressure ratio (*ru*) decreased from 1 in loose sand to 0.55 in dense sand under similar conditions. Foundation settlement was reduced from up to 9 mm in the most critical configuration to under 0.5 mm in the best-performing configurations. The density–settlement relationship was not monotonic: medium-dense sand ($Dr = 0.40$) produced the largest settlement in some configurations, while loose sand ($Dr = 0.30$) performed well when column length was sufficient. This study advocates for a minimum relative density of 0.50 for clean sands in regions anticipating strong, prolonged shaking akin to the Kocaeli earthquake. The results furnish empirical backing for performance-based ground improvement design in seismically active regions like Turkey's Marmara area.

Keywords: liquefaction; relative density; shaking table; earthquake; deep mixing; pore water pressure

Academic Editor: Anna Chiaradonna

Received: 2 September 2026
Revised: 21 October 2026
Accepted: 24 October 2026
Published: 28 October 2026

Copyright: © 2026 by the authors. Licensee MDPI, Basel, Switzerland. This article is an open access article distributed under the terms and conditions of the Creative Commons Attribution (CC BY) license.

1. Introduction

The 1999 Kocaeli (İzmit) earthquake in Turkey left behind clear evidence of what liquefaction can do to the ground and to buildings. In Adapazarı, investigators found severe ground failures, buildings tilting, and foundations sinking that were tied in part to liquefaction and cyclic softening of shallow saturated soils [1]. Similar damage showed up at the Hotel Sapanca site, where the earthquake triggered settlements and lateral ground movements [2]. Liquefaction happens when earthquake shaking raises pore-water pressure in saturated, susceptible soils, which drops the effective stress and weakens the soil's ability to resist shear deformation [3–5]. These events make it clear why liquefaction hazards need to be evaluated and mitigated in seismic regions like Turkey.

Densification is one of the main ways engineers reduce liquefaction risk in granular soils. Methods like vibro-compaction and dynamic compaction work by rearranging and packing soil particles more tightly, which raises penetration resistance and cyclic resistance and makes loose deposits less likely to liquefy [6,7]. The link between soil density and liquefaction resistance is well documented in both laboratory testing and field-based assessments [3,8]. However, determining the relationship between a specific target relative density (*Dr*) and an engineering performance such as excess pore-water pressure, settlement, and cyclic deformation under a given earthquake motion is still a challenge. This especially applies when the soil carries structural loads and affects the whole soil-foundation-structure system.

Most of what we know about liquefaction triggering comes from cyclic laboratory tests and empirical relationships built from field case histories. The simplified framework developed by Seed and Idriss, later updated through the NCEER/NSF workshops, relies mainly on field measurements, SPT, CPT, and shear-wave velocity to estimate liquefaction resistance [3,9]. These methods are essential in practice, but they can't reproduce the integrated response of soil, foundations, and structures through an entire earthquake time history. Physical model testing fills that gap by letting us study the system under controlled conditions. In particular, 1-g shaking-table and centrifuge studies have been used to look at liquefaction-induced foundation settlement and soil–structure interaction [10–12].

The effects of relative density on liquefaction resistance have been studied for decades. Seed et al. developed widely used relationships based on field performance and standardized SPT resistance, and later studies have linked soil density and penetration resistance to both liquefaction triggering and post-earthquake deformation [8]. Tokimatsu & Seed showed that earthquake-induced settlement of sand depends on the cyclic stress ratio, maximum shear strain, SPT resistance, and earthquake magnitude [13]. Ishihara & Yoshimine took this further by relating post-liquefaction volumetric strain to sand density and the factor of safety against liquefaction, giving engineers a practical basis for estimating settlement [14].

Most of these approaches, though, focus on soil behavior at the element scale, field correlations, or free-field ground response. They don't directly show how specific laboratory-controlled relative densities, say 0.30, 0.40, and 0.50, affect a loaded soil–foundation–structure system under a full earthquake record. Physical modeling studies have made it clear that structural loading and foundation response matter. Liu & Dobry, for instance, studied a shallow foundation on liquefiable sand and looked at how densification beneath the foundation influenced seismic response and settlement [11]. Dashti et al. used centrifuge tests to examine the mechanisms behind earthquake-induced settlement of buildings with shallow foundations on liquefiable soils [12]. Field and centrifuge evidence also show that how well ground improvement works depends on the characteristics and depth of the improved zone [15].

The waveform of the input motion is another critical factor. Liquefaction doesn't just depend on peak acceleration; the duration and cyclic nature of the loading also play a role. That means when we interpret how saturated soil–structure systems respond in physical models, we need to be careful about how we select and scale the earthquake motions. Iai established similitude relationships for 1-g shaking-table tests involving saturated soil–structure–fluid systems, which give us a theoretical basis for making sense of model-scale dynamic response [10].

This research fills that gap through a series of controlled 1-g shaking-table experiments to see how relative density affects the seismic response of saturated sand. We looked at model foundations for 10- and 15-story structures and used the 1999 Kocaeli earthquake record. Three relative densities were tested: 0.30, 0.40, and 0.50. To capture the

system's behavior, we tracked four key measurements: how excess pore-water pressure builds up and dissipates (using the pore-pressure ratio, *ru*), how much the foundations settle, the shear stress–strain response, and the dynamic properties of the soil.

This study isn't trying to prove that denser sand resists liquefaction better; we already know that. The real contribution is experimental: measuring how specific relative densities affect a range of performance parameters in a coupled soil–foundation–structure system under a realistic earthquake record. By examining pore-pressure ratio, settlement, shear deformation, dynamic soil properties, and structural acceleration together, the study provides a clearer picture of how relative density influences both the development and consequences of liquefaction. Those results can then help engineers make performance-based decisions about what densification level makes sense for sites with similar seismic loading.

The aim is for these findings to take this fundamental understanding of density effects and change it into practical insights supported by data for performance-based design. This helps engineers choose suitable densification targets to meet particular performance objectives during a given seismic event.

The novelty of this study is not the general finding that denser sand is more resistant to liquefaction. Rather, it is the experimental measurement of how specific relative densities (Dr = 0.30, 0.40, and 0.50) affect a coupled soil–foundation–superstructure system under a realistic earthquake record. Most previous work has focused on element-scale tests, empirical field correlations, or free-field ground response. Shaking-table studies that combine improved liquefiable sand, different relative densities, cement–sand columns, and building models under the 1999 Kocaeli motion are still limited. This study helps fill that gap by linking relative density to pore-pressure ratio, settlement, shear deformation, and dynamic soil properties in the same experimental program.

2. Methodology

All tests used the same homogeneous sand profile; the only variables were relative density, column length, and input motion. This study measured how the relative density of saturated sand affects its resistance to liquefaction under realistic earthquake loading, using the 1999 Kocaeli earthquake as the reference event. The experimental program combined physical modeling on a 1-g shaking table, controlled soil preparation, and instrumented monitoring of pore pressure, settlement, and dynamic response.

2.1. Physical Modeling and Scaling Laws

The tests were carried out on a hydraulic uniaxial shaking table at Urmia University. The platform measures 2 m × 3 m, has a maximum payload of 5 tons, and can produce accelerations up to 1.5 g, frequencies up to 20 Hz, and displacements up to 240 mm. Two servo-controlled motors drive it and can operate independently or together, helping maintain uniform vibration across the platform. The shaking table can simulate both harmonic and real earthquake motions.

To keep the model's dynamic behavior consistent with prototype conditions, Iai's generalized similitude law for 1-g shaking table tests was used [10]. A geometric scale factor of $\lambda = 20$ was chosen, meaning each dimension in the model represents one-twentieth of its prototype value. This factor set the relationships for length, time, acceleration, stress, and the other parameters listed in Table 1.

https://doi.org/10.3390/geotechnics6040109

Table 1. Scaling Factors Used in the Shaking-Table Model (λ = 20).

Parameter	Symbol	Prototype/Model Scale Factor	Scale Factor Value (λ = 20)
Length	L	λ	20
Density	ρ	1	1
Acceleration	a	1	1
Stress	σ	λ	20
Shear strain	ε	$\lambda^{0.5}$	4.47
Pore-water pressure	u	λ	20
Displacement	d	$\lambda^{1.5}$	89.44
Shear modulus	G	$\lambda^{0.5}$	4.47
Frequency	f	$\lambda^{-0.75}$	0.1057
Time	t	$\lambda^{0.5}$	4.472
Permeability	k	$\lambda^{0.75}$	9.457
Rate of water flow	q	$\lambda^{0.75}$	9.457

This table shows the scaling factors used for the shaking table model, with a geometric scale factor of 20. It lists how each parameter—like length, stress, time, and displacement—is scaled from the prototype to the model. Length, stress, and pore pressure all scale by 20, while density and acceleration don't change. Shear strain and shear modulus scale by 4.47, displacement by 89.44, and time, permeability, and flow rate by 9.457.

The soil was placed inside a flexible laminar shear box with internal dimensions of 1.36 m × 0.86 m × 0.70 m. The box consists of 18 aluminum frames stacked vertically and separated by low-friction roller bearings. Each frame can slide horizontally, which allows the soil column to deform in shear and approximates free-field conditions. A 2 mm thick PVC geomembrane lines the inside to keep the soil saturated and prevent leakage. This type of laminar container has been used extensively in shaking table studies to reduce boundary reflections and produce realistic one-dimensional shear deformation [16–18].

The Iai scaling relationships (time scale factor = $\sqrt{\lambda}$) were then used to adjust this data's amplitude and timing, ensuring that the model accurately reflected the duration and frequency of the actual earthquake.

It should be noted that 1 g shaking table tests cannot satisfy all similarity requirements simultaneously. Under Iai's generalized similitude law [10], length, stress, and pore-water pressure scale by λ = 20; acceleration and density scale by 1; time scales by $\sqrt{\lambda}$ = 4.47; and shear strain and shear modulus scale by $\sqrt{\lambda}$ = 4.47. The main deviations from perfect similarity are in the stress state (the 1 g condition cannot reproduce prototype confining stresses), strain rate effects, and drainage path length. As a result, absolute values such as settlement in millimeters should not be directly extrapolated to prototype scale without correction. Relative comparisons between tests remain valid because the same scaling law was applied consistently throughout.

2.2. Soil Properties and Model Preparation

The liquefiable soil was Firuzkuh sand (Code 161), a clean, uniformly graded sand classified as SP under the Unified Soil Classification System. It was chosen because its properties are well documented and it has been used as a benchmark material in previous geotechnical studies [17,19]. The key index properties are summarized in Table 2.

Table 2. Physical Properties of Firuzkuh Sand (Code 161).

Property	Symbol	Value	Standard/Method	Notes
Specific gravity	G_s	2.658	(ASTM-D854, 2023) [20]	Provided by the supplier
Minimum void ratio	e_{min}	0.548	(ASTM-D4253, 2016) [21]	Uniformly graded sand
Maximum void ratio	e_{max}	0.874	(ASTM-D4254, 2014) [22]	Lose packing
Mean grain size	D_{50}	0.27–0.30 mm	(ASTM-D422, 2007) [23]	Fine to medium sand
Coefficient of uniformity	C_u	1.70–2.10	(ASTM-D6913, 2025) [24]	Estimated from the grading curve
Soil classification	–	SP (Poorly graded sand)	USCS	Non-plastic
Minimum dry unit weight	$\gamma_{d,min}$	14.9–15.3 kN/m³	Calculated	Based on e_{max}
Maximum dry unit weight	$\gamma_{d,max}$	17.6–18.1 kN/m³	Calculated	Based on e_{min}
Saturated unit weight	γ_{sat}	19.2–19.6 kN/m³	Estimated	Depends on *Dr*
Particle shape	_	Sub-rounded to rounded	Visual inspection	Natural silica sand

Table 2 lists the physical properties of Firuzkuh sand (Code 161). It includes specific gravity (2.658), minimum and maximum void ratios (0.548 and 0.874), mean grain size (0.27–0.30 mm), coefficient of uniformity (1.70–2.10), and soil classification (SP, poorly graded sand). Dry unit weights range from 14.9–15.3 kN/m³ (minimum) to 17.6–18.1 kN/m³ (maximum). The saturated unit weight is 19.2–19.6 kN/m³. Particle shape is sub-rounded to rounded. The table also lists the ASTM standard used for each test. The liquefiable layer was intentionally built as a homogeneous, uniform sand profile. No silt, clay, or gravel layers were included, and the same sand was used in every test. This was done to isolate relative density as the main variable. Natural deposits are usually layered and heterogeneous, so this uniform profile is an idealization, not a direct model of field conditions.

The main variable in this study was the initial relative density of the sand. Three target states were tested: loose (*Dr* = 0.30), medium-dense (*Dr* = 0.40), and medium-dense (*Dr* = 0.50). The soil profile consisted of a 200 mm dense base layer (*Dr* = 0.80) at the bottom, overlain by a 500 mm liquefiable layer placed in five 100 mm lifts. The base layer acted as a non-liquefiable substratum and helped reduce boundary deformation during shaking. Figure 1 shows this layered soil profile in cross-section.

The three relative-density levels were selected to provide a practical range from a loose condition (*Dr* = 0.30) through an intermediate condition (*Dr* = 0.40) to a higher-density condition (*Dr* = 0.50), as shown in Table 3. The intermediate state was included to examine the transition between predominantly contractive and more dilative behavior under cyclic loading. These values were selected to provide clear differences in soil state while keeping the experimental program manageable and maintaining consistent model preparation and loading conditions. The selected range should not be interpreted as covering the full spectrum of possible sand densities or as defining a unique density threshold for the transition from contractive to dilative behavior.

Sand placement followed the dry pluviation method. For each 100 mm lift, the required mass of sand was calculated using standard soil mechanics relationships [25]. Based on the target relative density, the masses were approximately 184 kg, 187 kg, and 191 kg for *Dr* = 0.30, 0.40, and 0.50, respectively. For the 200 mm base layer at Dr = 0.80, about 404 kg of sand was used. These values are summarized in Table 4. Each layer was compacted with a square steel rammer (150 mm × 150 mm) to achieve the target density without disturbing the layer below.

Sensors were installed after each layer was compacted, which avoided damage during compaction. The pore pressure transducers were fully saturated and embedded in the sand to ensure good contact with the pore fluid. Accelerometers were fixed firmly at the designated depths (160 mm and 500 mm) within the soil column. After completing the

soil layers and column installation, the model was saturated by introducing de-aired water from the bottom of the laminar box through a controlled supply system. A constant water head was maintained, and saturation continued until no air bubbles were observed in the outflow. See Figure 1.

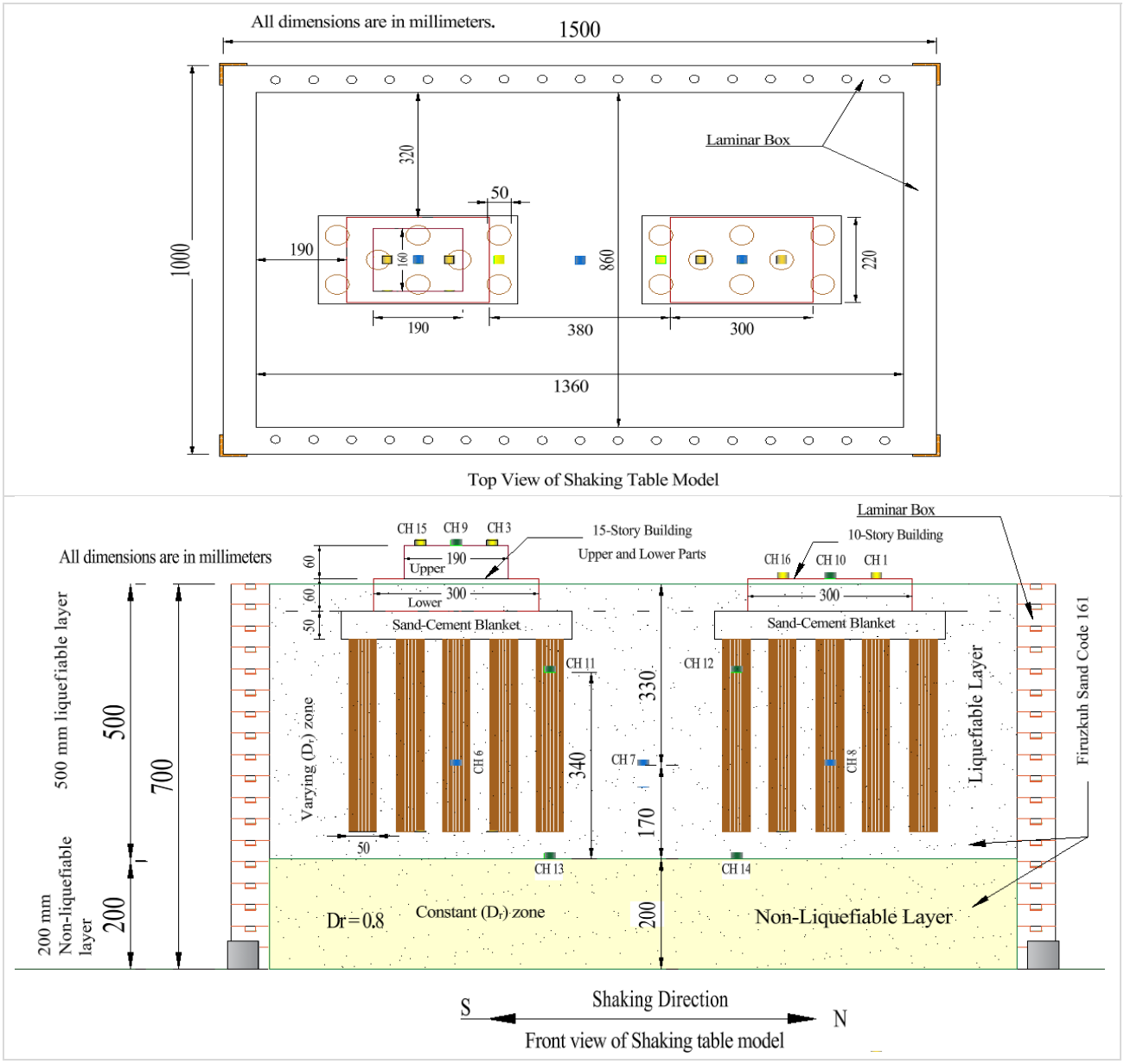


Figure 1. Top view and Front view schematic diagram of the complete physical model, detailing the soil layers, column placement, and the position of the 10-story and 15-story foundations on the sand-cement blanket.

Detailed Figure 1 cross-sectional schematic of the full physical model displaying the locations of the 10- and 15-story building foundations with instrument locations marked, the 500 mm thick layer of liquefiable sand, deep mixing columns of various lengths, and the 50 mm sand-cement blanket with the same cement ratio and water-cement ratio as used for the columns.

Table 3 lists all twelve shaking table tests one by one. For each test, it shows the group number, the relative density of the sand, the column length in centimeters, the input

motion, and which building models were used. Group 1 (Tests 1, 2, and 3) keeps the column length fixed at 390 mm and varies the relative density from 0.30 to 0.50. Test 1 used harmonic loading; Tests 2 and 3 used the Kocaeli 1999 record. Groups 2, 3, and 4 (Tests 4 through 12) each keep the relative density fixed—at 0.30, 0.50, and 0.40, respectively—and vary the column length across 150, 250, and 350 mm. All tests from Test 4 onward used the Kocaeli 1999 record, and every test used both the 10-story and 15-story building models.

Table 3. Test matrix for the twelve shaking table experiments. Each test is listed with its group, relative density, column length, input motion, and building models. Group 1 varies density at a constant column length; Groups 2–4 vary column length at constant.

Test No.	Group	*Dr(-)*	Column Length (mm)	Input Motion	Building Models
Test 1	1	0.3	390	Harmonic	10 & 15-story
Test 2	1	0.4	390	Kocaeli 1999	10 & 15-story
Test 3	1	0.5	390	Kocaeli 1999	10 & 15-story
Test 4	2	0.3	150	Kocaeli 1999	10 & 15-story
Test 5	2	0.3	250	Kocaeli 1999	10 & 15-story
Test 6	2	0.3	350	Kocaeli 1999	10 & 15-story
Test 7	3	0.5	150	Kocaeli 1999	10 & 15-story
Test 8	3	0.5	250	Kocaeli 1999	10 & 15-story
Test 9	3	0.5	350	Kocaeli 1999	10 & 15-story
Test 10	4	0.4	150	Kocaeli 1999	10 & 15-story
Test 11	4	0.4	250	Kocaeli 1999	10 & 15-story
Test 12	4	0.4	350	Kocaeli 1999	10 & 15-story

Table 4. Soil parameters and mass requirements for different relative densities.

D_r(-)	e(-)	γ (kg/m³)	γ (kN/m³)	H (m)	Mass (kg)
0.8	0.613	1730	16.97	0.20	404
0.5	0.711	1631	16.00	0.10	191
0.4	0.744	1600	15.70	0.10	187
0.3	0.776	1571	15.41	0.10	184

Table 4 shows soil parameters for four relative densities. It lists void ratio, unit weight (kg/m³ and kN/m³), layer thickness, and required sand mass.

2.3. Design and Fabrication of Cement-Stabilized Sand Columns

Cement–sand columns were used to represent deep mixing (DMM) elements. The mix design followed the same approach as the deep replacement columns described in the companion study, with a cement content of 110 kg/m³ of sand and a water-to-cement ratio of 1:1.33. These proportions were chosen based on previous laboratory work at Urmia University and standard deep mixing practice [17,26,27].

The installation sequence was as follows. First, sand was placed up to the bottom elevation of the columns using dry pluviation. Then, a triangular template was used to mark the column locations, as shown in Figure 2. PVC pipes (50 mm diameter) were inserted vertically into the sand at the marked positions to create guide holes. Sand placement continued in layers until the model box was filled to the target height. After that, the PVC pipes were carefully removed, leaving cylindrical cavities in the sand. The pre-mixed sand–cement slurry was then poured into the cavities in stages, with each stage compacted by tapping with a steel rod. The columns were arranged in a triangular pattern with a spacing of 170 mm between column centers and a replacement area ratio of

approximately 18.2%, following the layout used in the companion study [17]. Figure 2 shows the triangular arrangement template used to mark the column positions.

It should be noted that the columns were constructed using the deep mixing method, specifically in-situ mixing of sand with cement followed by a seven-day curing period. In the classification of soil improvement methods, this technique is similar in nature to the deep replacement method, as a prepared sand-cement material was placed into pre-formed cavities within the sand bed. This differs from field deep mixing, where the binder is mechanically mixed with the native soil in situ. The model columns therefore have a sharper column-soil interface and more uniform cement distribution than field columns. These differences may affect interface friction and stiffness. The columns should be seen as representing the overall stiffness and drainage function of deep mixing elements, rather than replicating the exact construction process.

The completed columns were left to cure for 7 days under a plastic cover at room temperature (22–25 °C). This curing period follows standard laboratory practice for cement-treated soils, which typically reach about 70% of their 28-day strength after one week [28].

The unconfined compressive strength (UCS) and modulus of the cement-sand column material were not measured in this study. Based on published correlations for cement-treated sands with similar mix proportions (110 kg/m^3 cement, w/c = 1:1.33), the expected 7-day UCS is approximately 0.5–1.0 MPa. This is at the lower bound of field deep-mixing columns, which typically range from 1 to 3 MPa. The model columns were intended primarily to improve drainage and provide lateral confinement, rather than to act as structural load-bearing elements. However, the absence of direct strength measurements is a limitation, and future studies should characterize the column material to better assess how well the model represents field conditions.

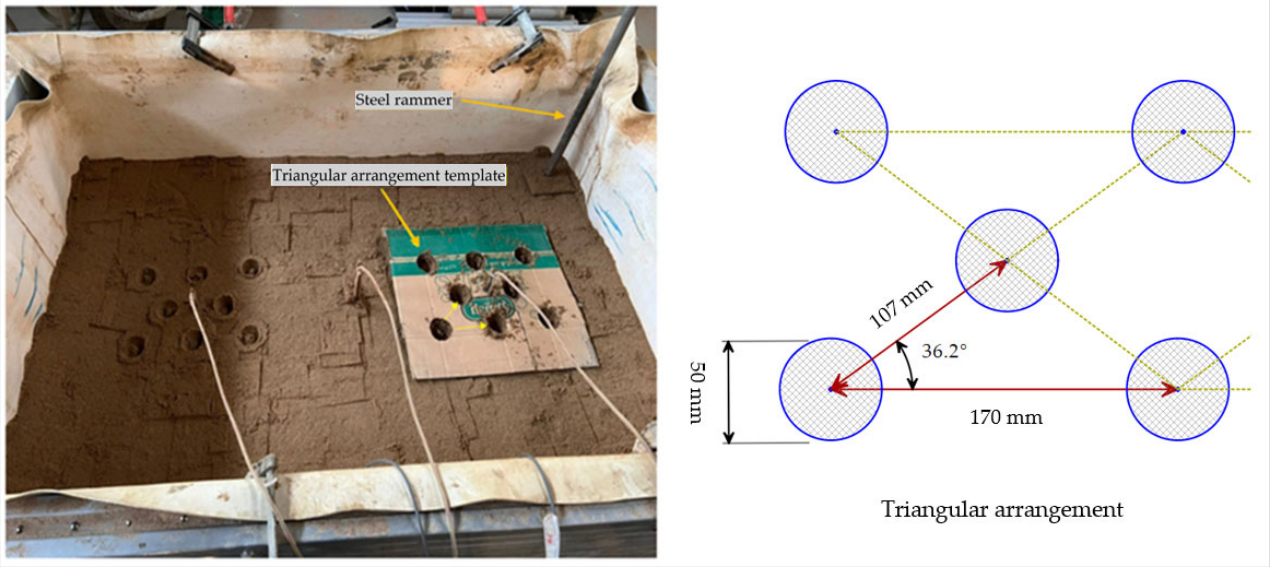


Figure 2. Triangular arrangement template used to mark the precise locations for installing the model columns.

Figure 2 shows a triangular template on the ground. The template is a grid used to mark the locations where model Cement-Stabilized Sand Columns will be placed in the shaking table experiment.

2.4. Surface Improvement and Structural Models

A 50 mm thick sand–cement blanket was placed on top of the improved ground to spread the foundation loads evenly across the columns and the surrounding soil. The blanket used the same mix as the columns (110 kg/m^3 cement, w/c = 1:1.33) and was cured for 3 days before testing. The blanket served two purposes: it acted as a working platform that distributed contact stresses, and it prevented local punching failure at the column heads [29].

Two scaled building models were placed on the blanket. The 10-story model was a single cast-iron block measuring 300 mm × 220 mm × 60 mm and weighing 30 kg. The 15-story model consisted of two stacked blocks: a lower block of 30 kg (300 mm × 220 mm × 60 mm) and an upper block of 15 kg (190 mm × 16 mm × 60 mm), giving a total of 45 kg. Both models were centered over their respective column groups to avoid eccentric loading. Figure 3 shows how the upper and lower cast-iron blocks were assembled to form the foundation models, and Figure 1 shows their position on the sand–cement blanket in the complete model setup. The weights and dimensions follow Iai's similitude law and represent low-rise and mid-rise buildings typical of the Marmara region.

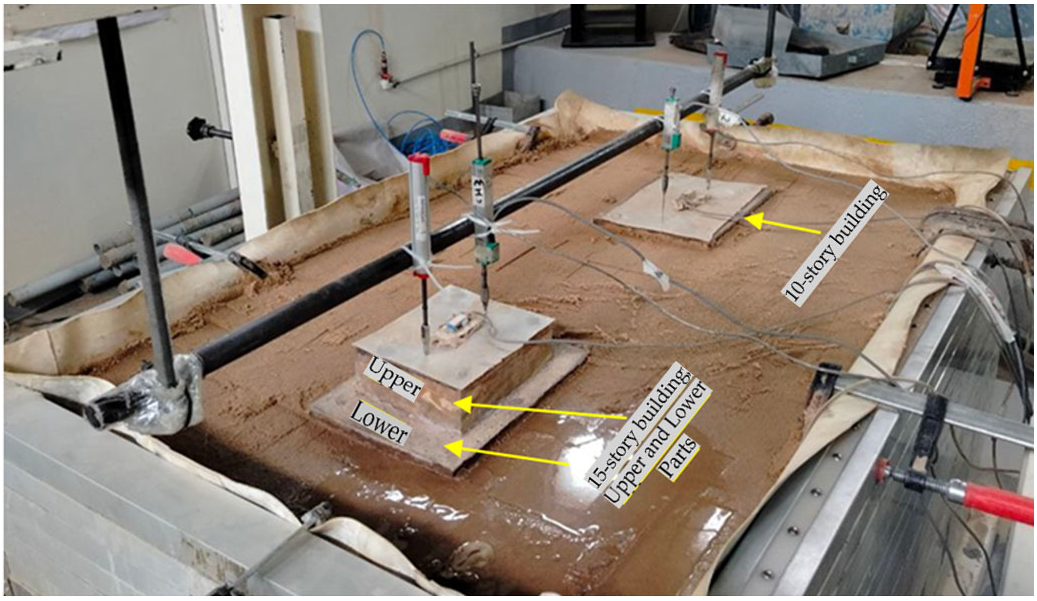


Figure 3. Assembly of the upper and lower cast-iron blocks that form the multi-story building foundations.

Figure 3 displays the construction of scaled models for shaking table tests. These models, representing the foundations of 10- and 15-story buildings, are assembled from stacked cast-iron blocks.

2.5. Soil Preparation and Saturation

The sand was placed using the dry pluviation method to achieve the target relative densities (Dr = 0.3, 0.4, 0.5, and 0.8). For each layer of 100 mm thickness, compaction was applied using a square steel hammer (150 mm × 150 mm); see Figure 2. According to the data in Table 2, compaction of 100 mm layers should proceed at relative densities of 0.3, 0.4, and 0.5 until 184, 187, and 191 kg of sand have been placed, respectively. For a relative density of 0.8, with a thickness of 200 mm, 404 kg of sand should be placed. Sensors (accelerometers, pore pressure transducers, LVDTs) were installed after each layer was compacted to avoid damage during compaction. The pore pressure sensors were fully saturated and embedded in sand to ensure good contact with the pore fluid.

Accelerometers were firmly fixed at given depths (160 mm and 50 mm) in the soil column. After completing the soil layering and column installation, the model was saturated by introducing de-aired water from the bottom of the laminar box through a controlled water supply system. A constant water head was maintained to ensure full saturation. The saturation process continued until no air bubbles were observed in the outflow.

2.6. Experimental Test Program and Test Matrix

Table 3 shows the group setups, along with column length and density tests. The experiments compared various conditions where relative density was the only changing factor. Table 2 shows soil details and the needed mass to get the desired densities. Table 3 presents the test matrix employed for the column length research (Groups 2, 3, and 4). Each test had the same setup: soil was placed to reach the target relative density, then saturated, sensors were placed, and the structure was put in position. Then, the same scaled Kocaeli motion was used as input. After getting data, the pore pressure ratio, settlement over time, and shear stress/strain were calculated using acceleration data [30–32]. The shear modulus (G) and damping ratio (λ) were found from stress-strain loops [33]. Table 4 lists the void ratio, bulk unit weight, layer thickness, and the mass of Firuzkuh sand required to achieve each target relative density in the model. These values were calculated based on the index properties given in Table 2 (specific gravity and maximum and minimum void ratios).

2.7. Input Ground Motion

The input motion was the N–S component of the YARIMCA station record (KOERI330) from the 1999 Kocaeli (İzmit) earthquake (Mw = 7.4). The record was obtained from the PEER NGA-West2 Ground Motion Database [34]. It was selected because of its strong near-fault pulse, long-duration shaking, and documented ability to trigger liquefaction. The record has a peak ground acceleration (PGA) of approximately 0.32 g and a total duration of about 35 s. Table 4**Table** shows the acceleration time history of the record.

The 1999 Kocaeli record was selected as a consistent reference motion for the experimental program because it represents a strong recorded earthquake motion associated with documented liquefaction effects in the region. Using a single earthquake record also allowed the effects of relative density, column length, and foundation loading to be evaluated without introducing additional variability associated with different seismic records. However, the use of a single ground motion limits the generalization of the results. Earthquake motions with different amplitudes, durations, frequency contents, and cyclic characteristics may produce different levels of pore-water-pressure generation and foundation deformation. Therefore, the quantitative responses obtained in this study should be interpreted in relation to the selected Kocaeli input rather than as universal responses for other earthquake motions.

The record was time-scaled and filtered according to Iai's similitude relationships. A band-pass filter between 0.05 and 15 Hz was applied to remove numerical drift and high-frequency noise before integration.

Figure 4 shows the acceleration time series of the 1999 Kocaeli (Turkey) earthquake recorded at the YARIMCA (KOERI330) station. The horizontal axis is time in seconds, and the vertical axis is acceleration in units of g (gravitational acceleration). The record has a total duration of approximately 35 s, with a peak ground acceleration (PGA) of approximately 0.32 g at the beginning. The waveform exhibits high-frequency content, with several prominent cycles typical of near-fault ground motion, which can initiate soil liquefaction.

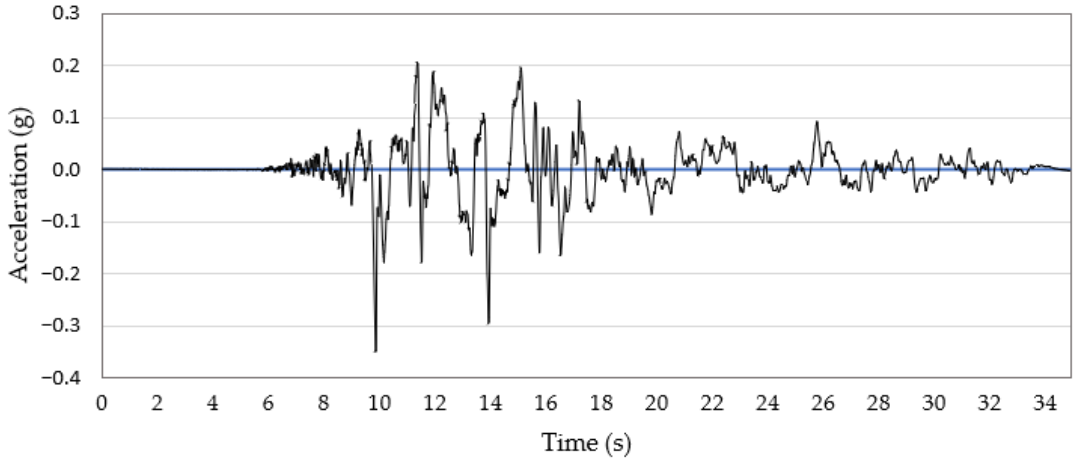


Figure 4. Acceleration time history of the 1999 Kocaeli (Turkey) earthquake recorded at the YARIMCA (KOERI330) station. The figure was prepared by the authors based on the earthquake record obtained from the PEER NGA-West2 Ground Motion Database [34].

2.8. Instrumentation and Data Collection

A total of thirteen sensors were used to capture the system's time-varying response throughout each test. Table 5 lists the instrumentation and channel mapping, and Figure 1 shows the complete sensor layout within the physical model.

Figure 1 presents the top and front views of the laminar box (1.36 m × 0.86 m), along with the two building foundations. The 15-story foundation sits on the left side and consists of two stacked cast-iron blocks: a lower block (300 mm × 220 mm × 60 mm, 30 kg) and an upper block (190 mm × 160 mm × 60 mm, 15 kg). The 10-story foundation sits on the right side as a single block (300 mm × 220 mm, 30 kg). Beneath both foundations, deep replacement columns are arranged in a triangular grid (small circles, 50 mm diameter, eight columns per side). The soil profile consists of a 200 mm dense base layer (Dr = 0.8), a 500 mm liquefiable sand layer (Dr = 0.3, 0.4, or 0.5), and a 50 mm sand–cement blanket.

The sensor positions are color-coded in Figure 1:

- LVDTs (■: CH1, CH3, CH15, CH16) were mounted 50 mm from the corners of each foundation to measure vertical settlement.
- Pore-water pressure sensors (■: CH6, CH7, CH8) were installed at a depth of 330 mm inside the liquefiable layer. *CH6* sits under the 15-story building, *CH7* sits between the two buildings, and *CH8* sits under the 10-story building.
- Accelerometers (■: CH11, CH12, CH13, CH14) were embedded within the soil mass at two depths: *CH11* and *CH12* at 160 mm, and *CH13* and *CH14* at 500 mm.
- Accelerometers CH9 and CH10 were mounted on the tops of the 15-story and 10-story building models, respectively.

The instruments themselves had the following specifications: accelerometers with a sensitivity of approximately 1000 mV/g, a measurement range of ±2 g, and a frequency response of 0–50 Hz; pore pressure transducers with a range of 0–100 kPa and an accuracy of ±0.25% full scale; and LVDTs with a range of ±50 mm and a resolution of 0.01 mm. All data (acceleration, pore pressure, and displacement) were recorded simultaneously using a 16-channel ART-DL16D dynamic data acquisition system at a sampling frequency of 1000 Hz. Figure 5 shows the actual placement of the accelerometers (CH9 and CH10) and the LVDTs (CH15, CH3, CH16, CH1) on the model surface and building foundations.

The pore-water-pressure transducers (CH6, CH7, and CH8) have a measurement range of 0–100 kPa and can only record positive pressures. They therefore cannot capture

negative pore-water pressures (suction), which may develop when dense sands dilate under cyclic shear. This limitation is particularly important for the *Dr* = 0.50 condition, where the soil can alternate between contractive and dilative phases during shaking. During dilation, suction would temporarily increase effective stress and contribute to liquefaction resistance, but because the transducers cannot read below zero, that part of the response is missing from the records. The (*ru*) values reported for *Dr* = 0.50 should therefore be treated as positive-pressure measurements rather than a complete pore-pressure history. They may overestimate the positive pressure buildup or, at minimum, fail to show the suction that helped limit liquefaction. This does not change the main comparative trends—denser sand still produced lower (*ru*) and less settlement—but it does mean the mechanism by which dense sand resists liquefaction cannot be fully quantified from these tests. The sensors remain adequate for tracking positive excess pore pressure and identifying liquefaction, which was the primary objective. Nevertheless, the *Dr* = 0.50 results should be interpreted with this constraint in mind.

Table 5. Instrumentation and channel mapping.

Channel	Sensor Type	Location/Depth	Schematic Symbol	Purpose
CH1	LVDT 1	Right side of a 10-story building	■ (yellow)	Settlement
CH16	LVDT 2	Left side of the 10-story building	■ (yellow)	Settlement
CH3	LVDT 3	Right side of a 15-story building	■ (yellow)	Settlement
CH15	LVDT 5	Left side of the 15-story building	■ (yellow)	Settlement
CH6	PWP 6	Under 15-story, z = 330 mm	■ (blue)	Pore pressure
CH7	PWP 7	Center of model, z = 330 mm	■ (blue)	Pore pressure
CH8	PWP 8	Under 10-story, z = 330 mm	■ (blue)	Pore pressure
CH9	ACC 9	Top of a 15-story building	■ (green)	Acceleration
CH10	ACC 10	Top of a 10-story building	■ (green)	Acceleration
CH11	ACC 11	Under 15-story, z = 160 mm	■ (green)	Acceleration
CH12	ACC 12	Under 10-story, z = 160 mm	■ (green)	Acceleration
CH13	ACC 13	Bed under 15-story, z = 500 mm	■ (green)	Acceleration
CH14	ACC 14	Bed under 10-story, z = 500 mm	■ (green)	Acceleration

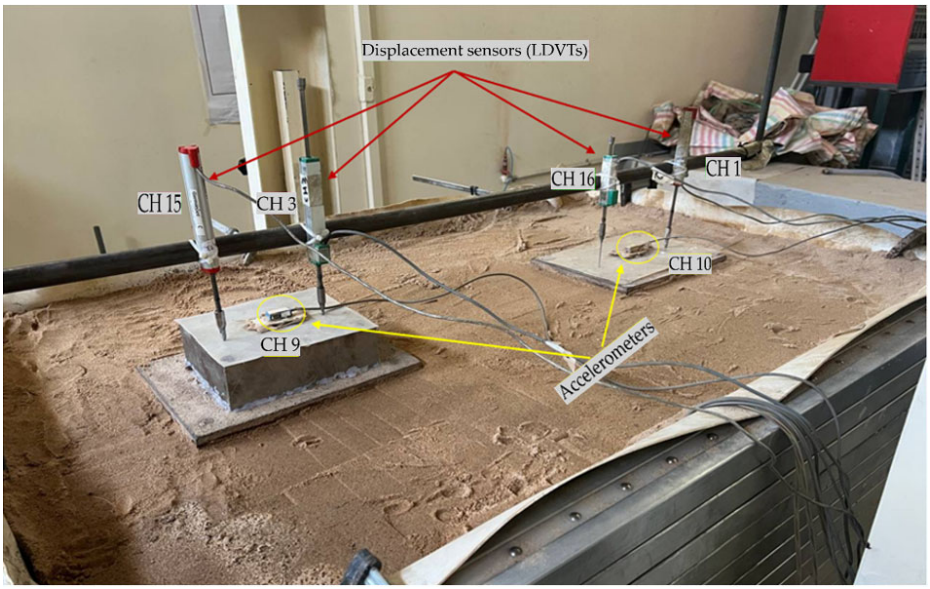


Figure 5. Placement of accelerometers (CH9, CH10) and displacement sensors (LVDTs: CH15, CH3, CH16, CH1) on the model surface and building foundations.

A table of thirteen sensors: four LVDTs for settlement, three pore pressure transducers at 330 mm depth, and six accelerometers at roof, mid-depth, and bed levels. Color-coded symbols match the figures.

Figure 5 illustrates the actual placement of instruments on the model surface and building foundations. We mounted accelerometers CH9 and CH10 on the 10-story and 15-story building models and placed LVDT displacement sensors CH15, CH3, CH16, and CH1 at the sides of the buildings to measure vertical settlement during shaking.

2.9. Verification of Liquefaction Potential Using the Simplified Procedure

To ensure the experimental model reflected a liquefiable situation, we calculated the Cyclic Stress Ratio (*CSR*) for the unimproved loose-sand reference case (*Dr* = 0.30, no columns) using the simplified procedure of Seed & Idriss [35], as updated by Youd et al. [3]. The *CSR* was calculated using Equation (1).

$$CSR = 0.65\left(\frac{a_{max}}{g}\right)\left(\frac{\sigma_{vo}}{\sigma'_{vo}}\right)r_d \quad (1)$$

where:

CSR = Cyclic Stress Ratio (the seismic demand)
σ_{vo} = Total vertical overburden stress at the depth of interest
σ'_{vo} = Effective vertical overburden stress at the depth of interest
a_{max} = Peak horizontal acceleration at the ground surface (in units of gravity, g)
g = Acceleration due to gravity
r_d = Stress reduction coefficient (a dimensionless factor ≤ 1.0)
For prototype depth 6.6 m (0.33 m × λ = 20), using γ_{sat} = 15.41 kN/m^3, *PGA* = 0.32 g:

- Saturated Unit Weight Correction

The saturated unit weight for *Dr* = 0.30 was calculated using Equation (2) and the index properties from Table 2:

$$\gamma_{sat} = \frac{G_s + e}{1 + e}\gamma_w \quad (2)$$

- Specific gravity: $G_s = 2.658$
- Void ratio at *Dr* = 0.30: $e = 0.776$
- Unit weight of water: $\gamma_w = 9.81$ kN/m^3

$$\gamma_{sat} = \frac{G_s + e}{1 + e}\gamma_w = \frac{2.658 + 0.776}{1 + 0.776} \times 9.81 = 19.0 \text{ kN/m}^3$$

For consistency with the saturated unit weight range reported in Table 2 (19.2–19.6 kN/m^3), the lower-bound value of 19.2 kN/m^3 was adopted. The CSR was calculated using Equation (1).

Parameter	Calculation	Value
σvo	19.2 × 6.6	126.7 kPa
u	9.81 × 6.6	64.7 kPa
$\sigma vo'$	126.7−64.7	62 kPa
rd	1.0−0.00765 × 6.6	0.95

$$CSR = 0.65\left(\frac{a_{max}}{g}\right)\left(\frac{\sigma_{vo}}{\sigma'_{vo}}\right)r_d = 0.65 \times 0.32 \times \left(\frac{126.7}{62}\right) \times 0.95 = 0.4$$

The factor of safety against soil liquefaction (*FS*) is calculated by comparing the soil's resistance to earthquake-induced loading with the stress caused by the earthquake. The *FS* was calculated using Equation (3).

$$FS = \frac{CRR}{CSR} \quad (3)$$

where:

1. FS = Factor of safety against soil liquefaction.
2. CRR = Cyclic Resistance Ratio, representing the soil's resistance to liquefaction during earthquake shaking.
3. CSR = Cyclic Stress Ratio, representing the cyclic shear stress imposed on the soil by earthquake loading.

For $Dr = 0.30$ and, $CRR \approx 0.12$.

$$FS = \frac{CRR}{CSR} = \frac{0.12}{0.40} = 0.3 < 1 \quad (4)$$

This indicates a very high susceptibility to earthquake-induced liquefaction under the considered seismic loading conditions [3].

- Comparison with Experimental Observations

The closest experimental case to the unimproved loose sand reference is Test 4 ($Dr = 0.30, L = 150$ mm), which used the shortest columns and therefore provided minimal improvement. Tables 7 and 8 show that in Test 4, the pore-pressure ratio (*ru*) was approximately 1.0 at all sensor locations (0.98, 1.1), confirming that liquefaction occurred. This is consistent with the analytical prediction of $FS < 1.0$.

For the improved case with long columns, Test 6 ($Dr = 0.30, L = 350$ mm) shows (ru) values of 0.34 and 0.57—all below 1.0—indicating that liquefaction was prevented. Settlements were also negligible (maximum −0.22 mm), confirming successful mitigation. See Table 6

Table 6. Comparison of liquefaction mitigation performance in unimproved and improved loose sand conditions

Loose sand, minimal improvement ($\boldsymbol{Dr = 0.30, L = 150}$ mm, Test 4)	$\boldsymbol{FS = 0.30 < 1.0}$ (Liquefaction expected)	$\boldsymbol{ru = 0.98 - 1.0}$, confirming liquefaction. Settlements: +2 mm, +9 mm (heave), −1.2 mm, −0.7 mm.	✓ Yes
Loose sand, improved ($\boldsymbol{Dr = 0.30, L = 350}$ mm, Test 6)	Not directly applicable (composite ground)	$ru = 0.34 - 0.57$ (< 1.0), no liquefaction. Settlements: −0.06 mm, −0.22 mm, +0.2 mm.	✓ Mitigation successful

This verification justifies the validity of our experimental results and shows consistency between the physical modelling and the accepted empirical criteria for triggering liquefaction. The simplified procedure correctly predicted liquefaction for the loose sand condition, and the experimental results confirm that adequate column length ($L = 350$ mm) can prevent it.

This CSR/FS calculation is an analytical baseline for the unimproved condition; no experimental unimproved model was tested under the Kocaeli motion.

Table 7. The (*ru*) values for Loose Sand (*Dr* = 0.30), (Tests 1, 4, 5, and 6), Medium-Dense Sand (*Dr* = 0.40), (Tests 2, 10, 11, and 12), and Medium-Dense Sand (*Dr* = 0.50), (Tests 3, 7, 8, and 9).

Test No.	PWP Sensor, at Depth 0.33 m	*Dr*(-)	Column Length (mm)	*ru*(-)
Loose Sand (*Dr* = 0.30), (Tests 1, 4, 5, and 6)				
Test 1	Below 15-story building	0.3	390	0.01
Test 1	Between two buildings	0.3	390	0.01

Test 1	Below 10-story building	0.3	390	0.01
Test 4	Below 15-story building	0.3	150	0.98
Test 4	Between two buildings	0.3	150	0.99
Test 4	Below 10-story building	0.3	150	1.00
Test 5	Below 15-story building	0.3	250	0.98
Test 5	Between two buildings	0.3	250	1.00
Test 5	Below 10-story building	0.3	250	0.99
Test 6	Below 15-story building	0.3	350	0.34
Test 6	Between two buildings	0.3	350	0.98
Test 6	Below 10-story building	0.3	350	0.57
Medium-Dense Sand (*Dr* = 0.40), (Tests 2, 10, 11, and 12)				
Test 2	Below 15-story building	0.4	390	0.99
Test 2	Between two buildings	0.4	390	1.00
Test 2	Below 10-story building	0.4	390	0.99
Test 10	Below 15-story building	0.4	150	1.00
Test 10	Between two buildings	0.4	150	0.61
Test 10	Below 10-story building	0.4	150	0.64
Test 11	Below 15-story building	0.4	250	0.68
Test 11	Between two buildings	0.4	250	1.00
Test 11	Below 10-story building	0.4	250	1.00
Test 12	Below 15-story building	0.4	350	0.97
Test 12	Between two buildings	0.4	350	1.00
Test 12	Below 10-story building	0.4	350	0.99
Medium-Dense Sand (*Dr* = 0.50), (Tests 3, 7, 8, and 9)				
Test 3	Below 15-story building	0.5	390	0.85
Test 3	Between two buildings	0.5	390	0.98
Test 3	Below 10-story building	0.5	390	0.99
Test 7	Below 15-story building	0.5	150	0.85
Test 7	Between two buildings	0.5	150	1.00
Test 7	Below 10-story building	0.5	150	0.98
Test 8	Below 15-story building	0.5	250	0.55
Test 8	Between two buildings	0.5	250	0.87
Test 8	Below 10-story building	0.5	250	1.00
Test 9	Below 15-story building	0.5	350	0.68
Test 9	Between two buildings	0.5	350	1.00
Test 9	Below 10-story building	0.5	350	0.98

Table 8. Summary of settlement, pore-pressure ratio, stress, and strain results for all 12 shaking table tests.

No.	LVDT's Location	*Dr(-)*	SC, Cl (mm)	*ru(-)*	Set. (mm)	Stress (kPa)	Strain (%)
T1	LS of the 15-SB-(CH15)	0.3	390	0.01	−1.5	±0.008	±1
T1	RS of the 15-SB-(CH3)	0.3	390	0.01	−8	±0.008	±1
T1	LS of the 10-SB-(CH16)	0.3	390	0.01	−7	±0.006	±0.8
T1	RS of the 10-SB-(CH1)	0.3	390	0.01	−2	±0.006	±0.8
T2	LS of the 15-SB-(CH15)	0.4	390	0.99	−2.5	±0.007	±2
T2	RS of the 15-SB-(CH3)	0.4	390	0.99	−8	±0.007	±2
T2	LS of the 10-SB-(CH16)	0.4	390	0.99	−3	±0.007	±2
T2	RS of the 10-SB-(CH1)	0.4	390	0.99	−4	±0.007	±2
T3	LS of the 15-SB-(CH15)	0.5	390	0.85	0.5	±0.0025	±2
T3	RS of the 15-SB-(CH3)	0.5	390	0.85	−0.4	±0.0025	±2

T3	LS of the 10-SB-(CH16)	0.5	390	0.99	−2.7	±0.0025	±2
T3	RS of the 10-SB-(CH1)	0.5	390	0.99	−7	±0.0025	±2
T4	LS of the 15-SB-(CH15)	0.3	150	0.98	−1.2	±0.0025	±1
T4	RS of the 15-SB-(CH3)	0.3	150	0.98	−0.7	±0.0025	±1
T4	LS of the 10-SB-(CH16)	0.3	150	1	2	±0.003	±1
T4	RS of the 10-SB-(CH1)	0.3	150	1	9	±0.003	±1
T5	LS of the 15-SB-(CH15)	0.3	250	0.98	0.025	±0.0015	±2
T5	RS of the 15-SB-(CH3)	0.3	250	0.98	−0.27	±0.0015	±2
T 5	LS of the 10-SB-(CH16)	0.3	250	0.99	−0.2	±0.0015	±2
T5	RS of the 10-SB-(CH1)	0.3	250	0.99	−0.15	±0.0015	±2
T6	LS of the 15-SB-(CH15)	0.3	350	0.34	0.2	±0.002	±2
T6	RS of the 15-SB-(CH3)	0.3	350	0.34	−0.22	±0.002	±2
T6	LS of the 10-SB-(CH16)	0.3	350	0.57	−0.06	±0.002	±2
T6	RS of the 10-SB-(CH1)	0.3	350	0.57	−0.06	±0.002	±2
T7	LS of the 15-SB-(CH15)	0.5	150	0.85	−2	±0.004	±1
T7	RS of the 15-SB-(CH3)	0.5	150	0.85	−6.5	±0.004	±1
T7	LS of the 10-SB-(CH16)	0.5	150	0.98	−4.2	±0.005	±1
T7	RS of the 10-SB-(CH1)	0.5	150	0.98	−0.4	±0.005	±1
T8	LS of the 15-SB-(CH15)	0.5	250	0.55	−0.22	±0.0015	±1.5
T8	RS of the 15-SB-(CH3)	0.5	250	0.55	−3.5	±0.0015	±1.5
T8	LS of the 10-SB-(CH16)	0.5	250	1	−2	±0.0015	±1.5
T8	RS of the 10-SB-(CH1)	0.5	250	1	−0.5	±0.0015	±1.5
T9	LS of the 15-SB-(CH15)	0.5	350	0.68	0.2	±0.002	±2
T9	RS of the 15-SB-(CH3)	0.5	350	0.68	−7	±0.002	±2
T9	LS of the 10-SB-(CH16)	0.5	350	0.98	−4	±0.002	±2
T9	RS of the 10-SB-(CH1)	0.5	350	0.98	−0.5	±0.002	±2
T10	LS of the 15-SB-(CH15)	0.4	150	1	−1.2	±0.0015	±1
T10	RS of the 15-SB-(CH3)	0.4	150	1	−2.5	±0.0015	±1
T10	LS of the 10-SB-(CH16)	0.4	150	0.64	−2	±0.0015	±1
T10	RS of the 10-SB-(CH1)	0.4	150	0.64	−0.3	±0.0015	±1
T11	LS of the 15-SB-(CH15)	0.4	250	0.68	−2.3	±0.006	±2
T11	RS of the 15-SB-(CH3)	0.4	250	0.68	−14	±0.006	±2
T11	LS of the 10-SB-(CH16)	0.4	250	1	−9.5	±0.006	±2
T11	RS of the 10-SB-(CH1)	0.4	250	1	−0.5	±0.006	±2
T12	LS of the 15-SB-(CH15)	0.4	350	0.97	−0.1	±0.005	±2
T12	RS of the 15-SB-(CH3)	0.4	350	0.97	−6.5	±0.005	±2
T12	LS of the 10-SB-(CH16)	0.4	350	0.99	−1.5	±0.005	±2
T12	RS of the 10-SB-(CH1)	0.4	350	0.99	0	±0.005	±2

Note: T = Test; LS = Left Side; RS = Right Side; SB = story building, SC = Sand-Cement, *Dr* = Relative Density, CL = Column Length, Set. = Settlement. Table 8 is a summary of settlement, pore-pressure ratio (*ru*), stress, and strain for the shaking table tests. The table has eight columns: test number, LVDT location, relative density (*Dr*), column length, (*ru*), settlement in mm, stress in kPa, and strain in percent. Each test has four rows covering the left and right sides of the 15-story and 10-story building models. Negative settlement values mean upward movement, while positive values mean downward movement.

3. Results

It should be noted at the outset that every shaking-table test included cement–sand columns. Therefore, all comparisons in this section are among improved cases only. No physical unimproved benchmark test was performed; the unimproved condition is represented analytically by the CSR/FS calculation. The results should not be read as

showing what would happen on unimproved ground. They show how relative density and column length affect performance once some degree of improvement is already present.

For the remainder of the results, $ru = 1.0$ is used as the liquefaction-triggering threshold. In the revised calculations, the initial vertical effective stress was defined site-specifically for each test location using the corrected soil profile and unit weights. The computed *ru* values are therefore physically consistent: none exceeds 1.0, and the maximum value is 1. For engineering interpretation, $ru = 1.0$ is consequently treated as full liquefaction.

In loose sand (*Dr* = 0.30), the (*ru*) values quickly reached 0.99 to 1.0, which means full liquefaction happened. When *Dr* = 0.40, the highest values of *ru* reached 1 in several cases. Overall, the pressure build-up was much lower than in looser sands, but liquefaction was not completely prevented. We can find the exact (*ru*) data for these tests in Table 7 and Figure 6.

For Dr = 0.50, the transducers recorded only positive pore pressures, so any dilation-induced suction was missed. Thus, the (*ru*) reflects only the positive-pressure component and does not capture the full effective-stress response. The conclusion that denser sand performs better still holds, but exact (*ru*) values for dense sand should be interpreted with this limitation.

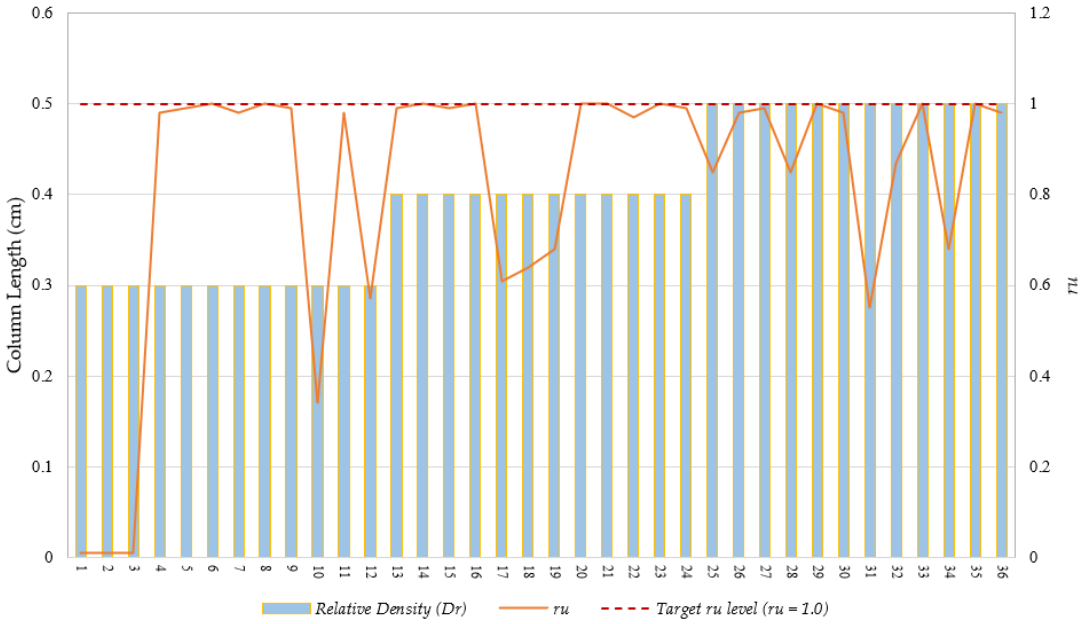


Figure 6. Pore pressure ratio (*ru*) values for Loose Sand (*Dr* = 0.30) (Tests 1, 4, 5, and 6) from No. 1 to 12, Medium-Dense Sand (*Dr* = 0.40) (Tests 2, 10, 11, and 12), and Medium-Dense Sand (*Dr* = 0.50) (Tests 3, 7, 8, and 9).

Figure 6 shows three grouped bar graphs of (*ru*) for three relative densities (*Dr* = 0.30, 0.40, 0.50). Left group: loose sand (Tests 1, 4, 5, 6). The middle group shows medium-dense sand (Tests 2, 10, 11, and 12). The right group is medium-dense sand (Tests 3, 7, 8, 9). For each test, three PWP sensor positions are shown: (i) under the 15-story building, (ii) between two buildings, and (iii) under the 10-story building. The horizontal dashed red line at *ru* = 1.0 represents the liquefaction threshold, where *ru* = 1.0 indicates full liquefaction (effective stress = 0). In general, longer columns (350–390 mm) produce lower

(*ru*) values, but shorter columns (150 mm) often exceed the liquefaction threshold, especially in loose and medium-dense sands.

Table 7 summarizes pore-water pressure ratio (*ru*) values from all shaking table tests, grouped by relative density (*Dr* = 0.30, 0.40, and 0.50) and column length. For each test, the (*ru*) is listed for three PWP sensors at 0.33 m depth: below the 15-story building (CH6), between the buildings (CH7), and below the 10-story building (CH8). The excess pore water pressure ratio (*ru*) ranges between 0.01 and 1.00, with maximum values observed across various experiments and sites. In general, the results indicate that the *ru* is influenced by factors such as relative density, column length, and building configuration. When *ru* approaches 1.00, the potential for liquefaction is high; conversely, at lower values, the increase in pore water pressure is more limited. All three pore-water pressure transducers (CH6, CH7, CH8) functioned properly in every test. The (*ru*) values reported in Table 7 represent the complete dataset for all sensors.

The (ru) values in Table 7 vary across the three sensor locations, even under the same test conditions. For example, in Test 8 (*Dr* = 0.50, L = 250 mm), the (ru) values were 0.55 below the 15-story building, 0.87 between the two buildings, and 1.00 below the 10-story building. These differences suggest that excess pore water pressure did not develop uniformly throughout the soil. This may be related to differences in stress conditions, drainage paths, and distances from the columns at each sensor location. To ensure a conservative evaluation of liquefaction potential, the highest (*ru*) value recorded by the three sensors is used for each test condition. However, because no repeat tests were conducted, the consistency of the measurements could not be evaluated.

Foundation Settlement: The tests also show that increasing the relative density (*Dr*) of the sand can help reduce settlement; however, this effect is not uniform across all measurement points. This trend corresponds to the settlement prediction models of [13,14,17]. You can see how the settlement changed over time for all the density tests in Table 8, which has all the displacement measurements from the LVDT sensors. The (*ru*) values for Test 1 in Table 7 are harmonic loading, not earthquake loading, and are all near zero. This study focuses on a real earthquake, showing that regular harmonic inputs (sine and cosine) have effects significantly smaller than those of an actual seismic event, such as the Kocaeli earthquake.

Group 1 settlement-time graphs (Figure 7), using a consistent column length of 390 mm. You can see how the displacement changed over time for all the density tests in Table 8, which has all the displacement measurements from the LVDT sensors: each test consists of four graphs. Loose sand (*Dr* = 0.3) in Test 1, as shown in Figure 7, shows a maximum displacement of approximately −20 mm and a final displacement of approximately −8 mm. Medium-dense sand (*Dr* = 0.4) in Test 2 exhibits a maximum displacement of approximately −11 mm and a final displacement of approximately −8 mm. Test 3, using Medium-dense sand (*Dr* = 0.5), recorded a maximum displacement of approximately −19 mm and a final displacement of approximately −7 mm. These tests illustrate how density affects settlement under building foundations.

The pore pressure ratio (*ru*) values were recalculated after identifying and correcting a spreadsheet error involving soil unit weights and layer depths. This error had led to an underestimation of the initial vertical effective stress and, consequently, unrealistically high (*ru*) values. The corrected results are presented in Tables 6 and 7. The results also show that settlement is not governed by the pore pressure ratio alone, as similar (ru) values can produce different settlements depending on the reinforcement configuration and local stress conditions. Higher pore pressure ratios in the unreinforced zone between the buildings indicate the influence of foundation interaction on the generation of pore

pressure. In general, the (*ru*) values approaching 1.0 signify the development of liquefaction conditions.

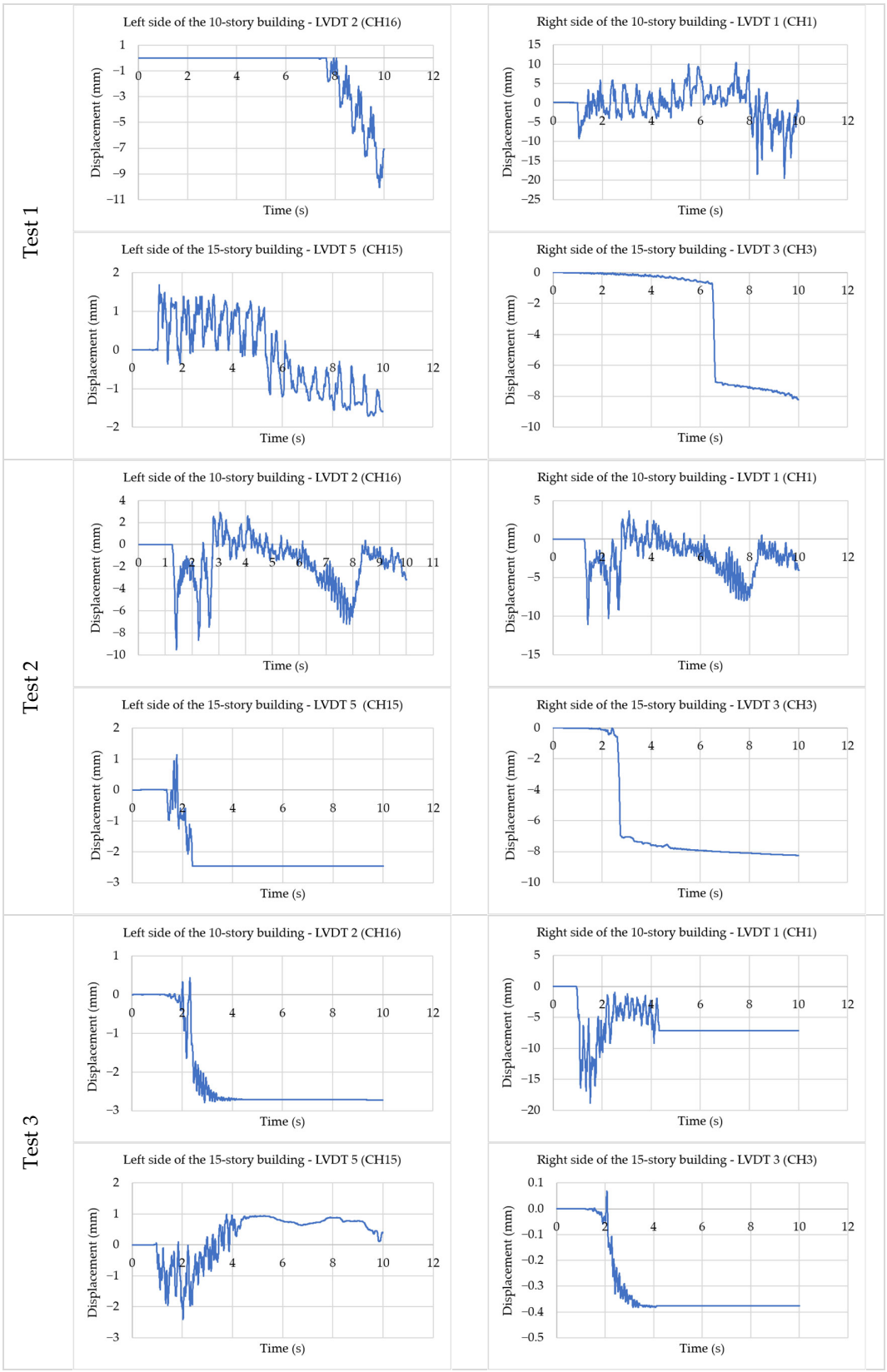


Figure 7. Timeline of the Foundations Settlement for group 1 (Test 1, Test 2, and Test 3).

Settlement values in Table 8 are model-scale measurements. They cannot be directly used for prototype engineering without applying the Iai's similitude relationships [10]. For $\lambda = 20$, the displacement scale factor is 89.44.

Under the sign convention used here, negative values in settlement represent upward movement, and positive values represent downward movement. For Test 12 (Dr = 0.40, L = 350 mm), the values −1.5 mm and −6.5 mm are negative, indicating upward displacement.

Soil Dynamic Properties: Significantly different behaviors were shown by shear stress-strain hysteresis loops. Large, pinched loops with significant stiffness loss were seen in loose sand (Figures 8 and 9). Dense sand displayed strong, elliptical loops with high stiffness retention and strains less than 1.5%. The G-γ plots of Figure 10 demonstrate how the secant shear modulus (G) at equivalent strain levels increased by a factor of 3 to 4 from Dr = 0.30 to Dr = 0.50 [33]. Structural Acceleration: A reduction effect was seen in the foundation-level acceleration response spectra. High-frequency accelerations were significantly reduced in loose, liquefied soil, while some low-frequency amplification resulted from the softening of the soil. A stiff, responsive soil profile was indicated by foundation accelerations in dense sand that more closely matched the input motion.

The shear modulus and damping values derived from the acceleration records carry estimated uncertainties of about ±15% and ±20%, respectively, because of double integration, filtering, and baseline correction. The fitted *Gmax* values in Table 8 and the degradation curves in Figure 10 should therefore be treated as approximate estimates rather than high-precision measurements.

It should be noted that the shear modulus and damping values reported here carry an estimated uncertainty of ±15% and ±20%, respectively, due to the integration and filtering procedures used to derive stress-strain loops from acceleration records. These uncertainties should be considered when comparing absolute values, although relative comparisons between tests remain valid because the same processing chain was applied throughout.

The shear stress distribution with depth was calculated from the acceleration records using the approach proposed by Zeghal and Elgamal [30] , as expressed inEquation (5).

$$\frac{\partial \tau}{\partial z} = \rho \ddot{u} \tag{5}$$

where the parameters ü and ϱ are the acceleration and density at depth, respectively. The shear stress at the desired depth is obtained by integrating with the Equation (6).

$$\tau(z) = \int \rho\,(z)\,\ddot{u}(z)\,dz \tag{6}$$

The time history of the ground acceleration can be obtained by nonlinear extrapolation of the acceleration data of the pair of sensors buried at depth using the Equation (7) [30].

$$\ddot{u}(z) = \ddot{u}_1 + \frac{\ddot{u}_2 - \ddot{u}_1}{z_2 - z_1}(z - z_1) \tag{7}$$

To calculate the shear strain, the displacement time history is obtained by integrating the acceleration time history twice. In the middle of the two acceleration sensors, the shear strain value is calculated by Equation (8) [30].

$$\gamma = \frac{u_2 - u_1}{z_2 - z_1} \tag{8}$$

The where γ is the shear strain, $(u_2 - u_1)$ are the horizontal displacements at depths (z_1) and (z_2), respectively, and $(z_2 - z_1)$ is the vertical distance between the two points.

The shear stress and strain derived from double integration of acceleration records are sensitive to baseline correction, filtering, and integration errors. In this study, a

consistent processing chain was applied to all tests: a band-pass filter between 0.05 and 15 Hz, baseline correction using a moving average, and double integration with linear interpolation between the two accelerometer locations. Based on a sensitivity analysis of these processing steps, the estimated uncertainty is approximately ±15% for the secant shear modulus (G) and ±20% for the damping ratio (D). The derived G values were compared with published data for Firuzkuh sand and similar clean sands [19], and the degradation trends are consistent. However, independent validation through element-scale cyclic triaxial or simple shear tests was not performed and is recommended for future work.

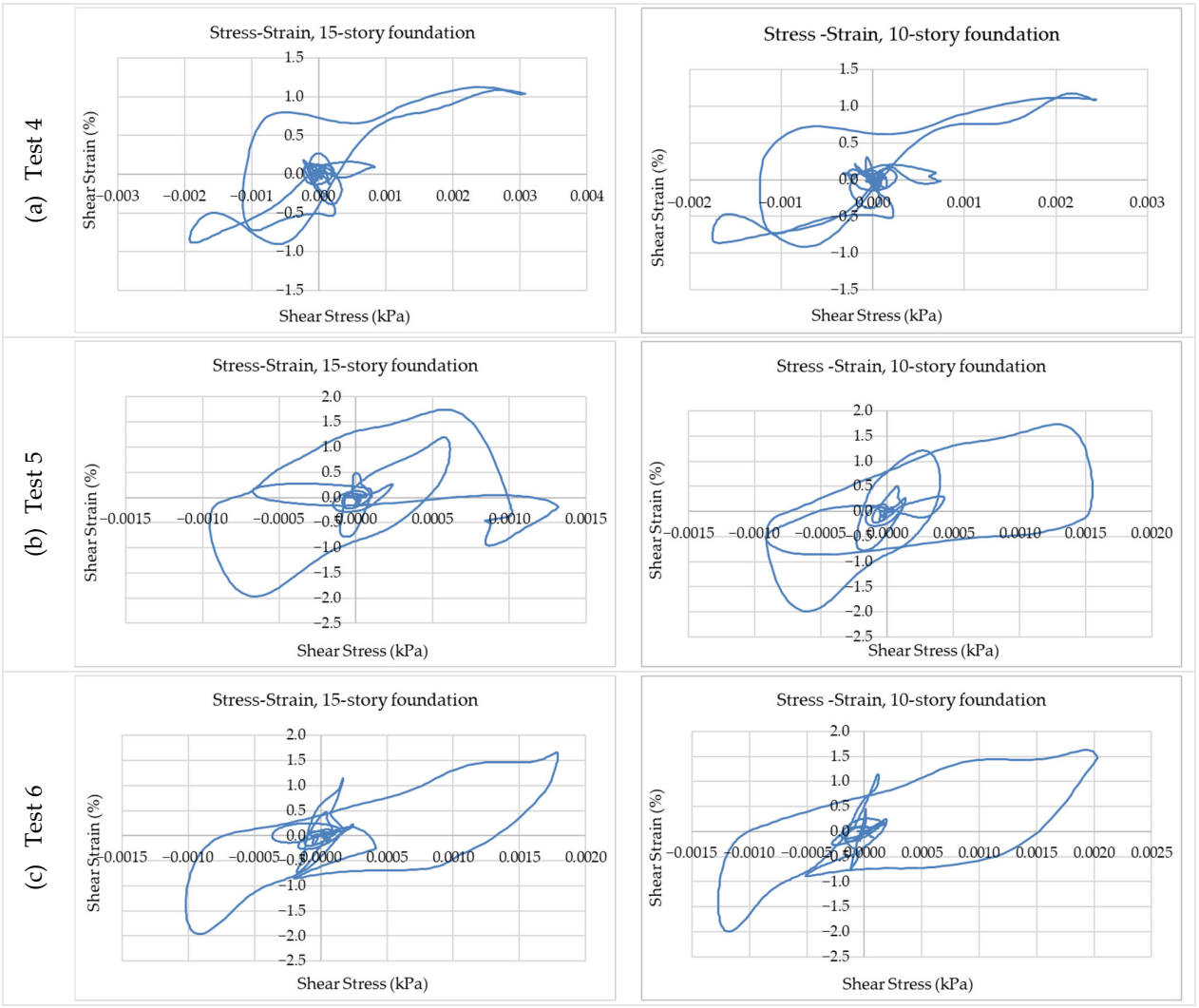


Figure 8. Effect of Column Length on Stress-Strain Behavior in Loose Sand (Dr = 0.3). Shear stress-shear strain hysteresis loops for column lengths of (**a**) 150 mm, (**b**) 250 mm, and (**c**) 350 mm, below 15-story and 10-story foundations.

In shear stress-strain tests on loose sand at a relative density of 0.3, the column length influenced the hysteresis loops. Short columns (150 mm) in Test 4 produced wide, pinched loops, which suggest low stiffness and a large decline in stiffness. Test 5, with medium columns (250 mm), showed moderately wide loops. Test 6, using long columns (350 mm), resulted in narrower loops. These results show how column length affects the shear of loose sand under loading that simulates 15-story and 10-story building foundations.

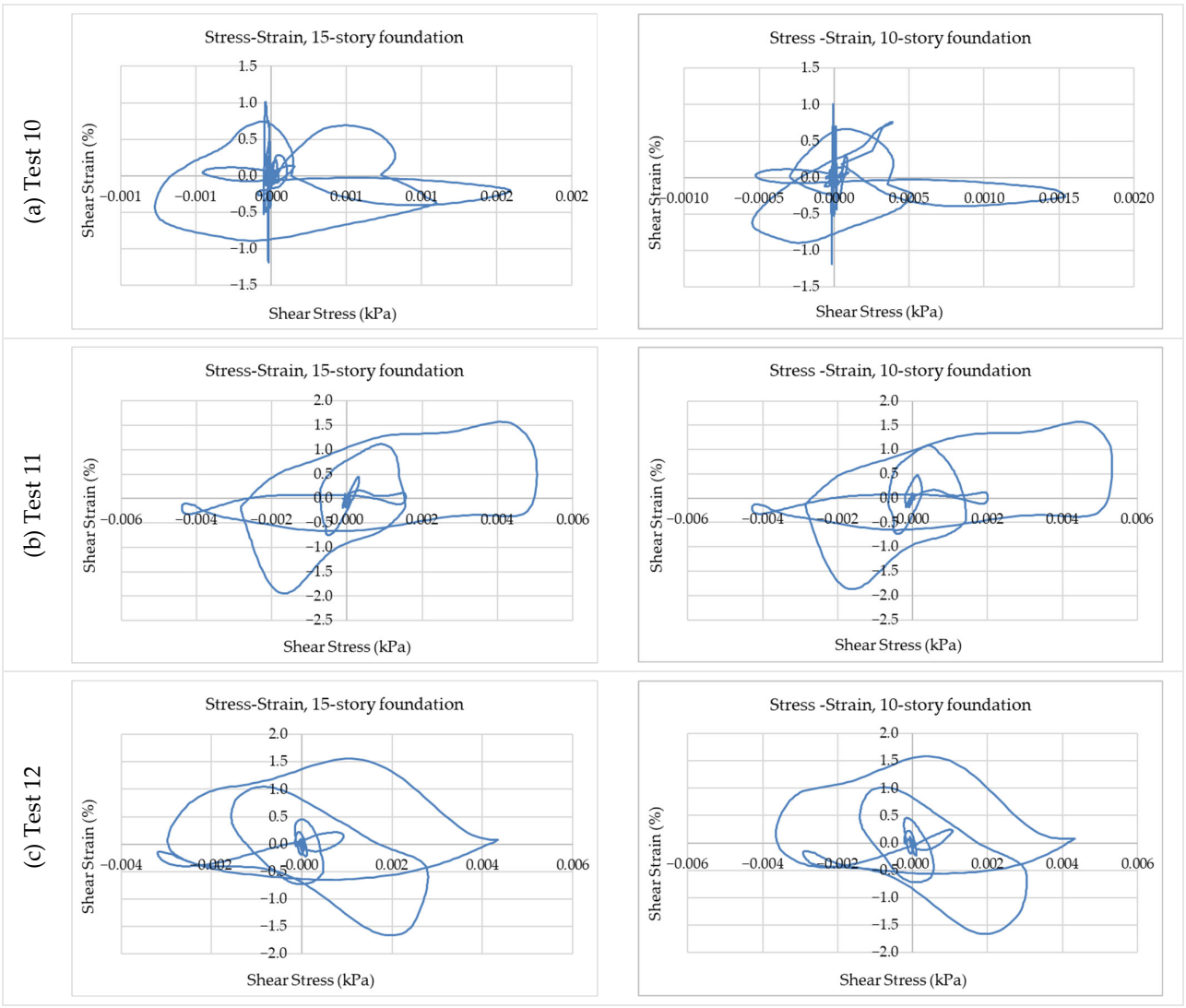


Figure 9. Effect of Column Length on Stress-Strain Behavior in Medium-Dense Sand (*Dr* = 0.4). Shear stress–shear strain hysteresis loops for column lengths of (**a**) 150 mm, (**b**) 250 mm, and (**c**) 350 mm below 15-story and 10-story foundations.

Shear stress-strain hysteresis loops were examined for medium-dense sand at a relative density of 0.4. Test 10, using short columns (150 mm), showed moderately wide loops; Test 11, with medium columns (250 mm), showed narrower loops; and Test 12, which used long columns (350 mm), showed the narrowest, most vertical loops. This indicates that composite stiffness increases as column length increases within medium-dense sand under 15- and 10-story foundations.

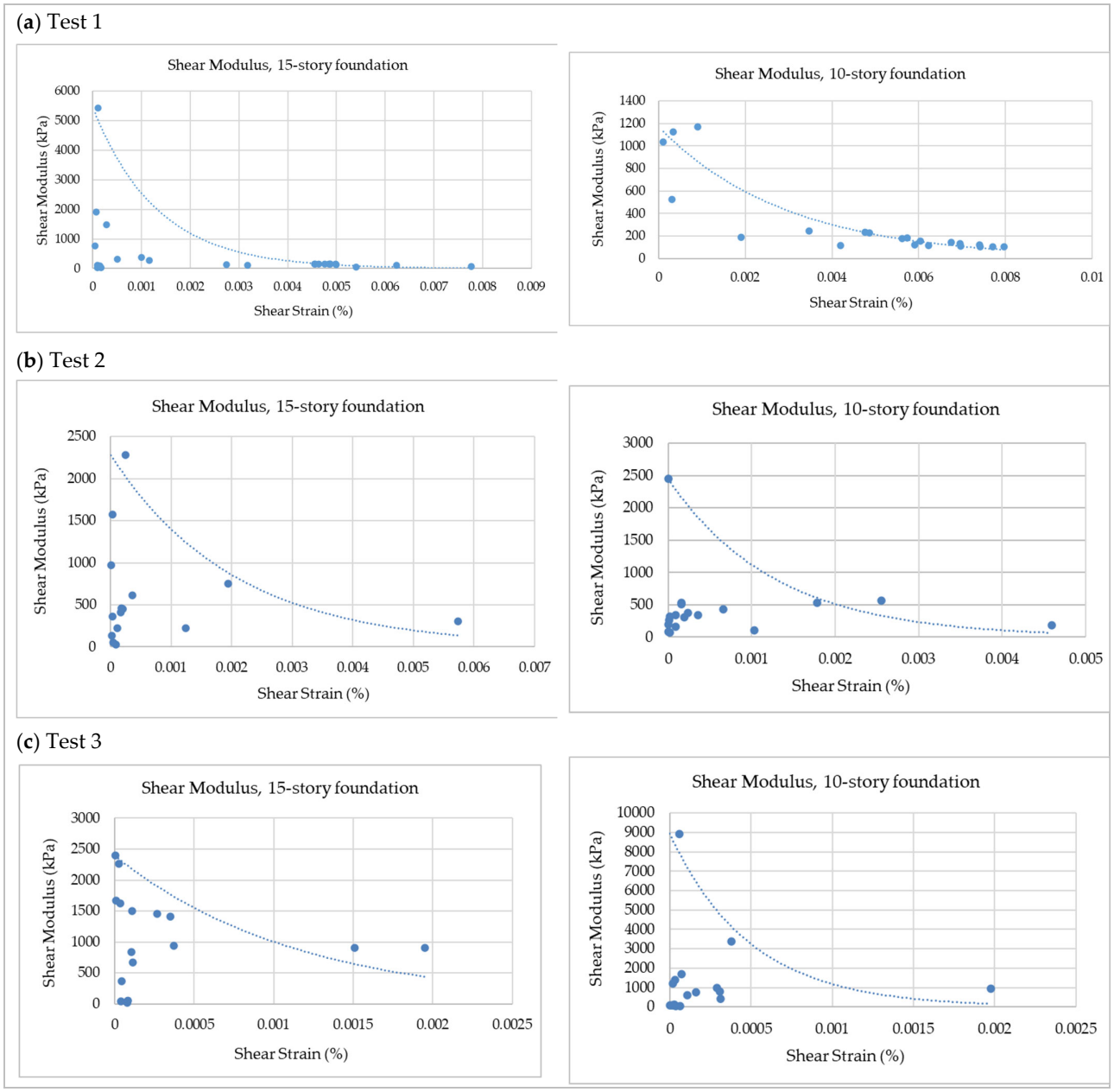


Figure 10. Shear modulus (G) versus shear strain (γ) for loose, medium-dense, and dense sand under different column lengths for Tests 1, 2, and 3. The authors prepared the figure from experimental data; they fitted the degradation curves using the Hardin–Drnevich hyperbolic model [33].

Figure 10 is a three-panel figure labeled a, b, and c. Each panel contains two side-by-side scatter plots: the left plot is for the 15-story foundation and the right plot is for the 10-story foundation. The horizontal axis is shear-strain in percent, and the vertical axis is shear-modulus in kPa. In panel a, the left plot has a vertical axis reaching 5500 kPa, and the right plot reaches 1200 kPa. In panel b, the left plot goes up to 2300 kPa and the right plot up to 2500 kPa. In panel c, the left plot reaches 2400 kPa and the right plot reaches 9000 kPa. In all plots, the scattered data points show a clear decreasing trend, with a dotted curve fitted through them. The figure compares shear modulus degradation with increasing shear strain for loose, medium-dense, and dense sand under different column lengths. G and damping values are derived from acceleration records and carry the uncertainties stated in the text. The fitted *Gmax* values are approximate.

The degradation curves in Figure 10 were fitted using the Hardin–Drnevich hyperbolic model, using Equation (9) [33].

$$G = \frac{G_m}{1 + \gamma/\gamma_r} \quad (9)$$

where G_{max} is the small-strain shear modulus and γ_r is the reference strain. The R^2 values for the fits range from 0.72 to 0.81, indicating a reasonable fit given the inherent scatter in the data. The scatter arises from spatial variability in sand density, localized drainage conditions, sensor placement effects, and integration errors. The ratio of G_{max} between Dr = 0.50 and Dr = 0.30 is approximately 3.5–4.0 for the 10-story foundation, but the increase is smaller for the 15-story foundation and depends on column length. A summary of G_{max} and R^2 values are given in Table 9.

Table 9. Fitted G_{max} and R^2 values for shear modulus degradation curves.

Test	Group	*Dr(-)*	*L* (mm)	Foundation	*Gmax* (kPa)	R^2
1	1	0.3	390	15-story	~5500	0.72
1	1	0.3	390	10-story	~1200	0.75
2	1	0.4	390	15-story	~2300	0.76
2	1	0.4	390	10-story	~2500	0.78
3	1	0.5	390	15-story	~2400	0.78
3	1	0.5	390	10-story	~9000	0.81
4	2	0.3	150	15-story	~2500	0.74
4	2	0.3	150	10-story	~7500	0.76
5	2	0.3	250	15-story	~12,000	0.79
5	2	0.3	250	10-story	~5000	0.77
6	2	0.3	350	15-story	~5000	0.78
6	2	0.3	350	10-story	~12,000	0.8
7	3	0.5	150	15-story	~2400	0.77
7	3	0.5	150	10-story	~1800	0.75
8	3	0.5	250	15-story	~3300	0.79
8	3	0.5	250	10-story	~2200	0.78
9	3	0.5	350	15-story	~6500	0.8
9	3	0.5	350	10-story	~7500	0.81
10	4	0.4	150	15-story	~3000	0.73
10	4	0.4	150	10-story	~2500	0.75
11	4	0.4	250	15-story	~4500	0.76
11	4	0.4	250	10-story	~2200	0.75
12	4	0.4	350	15-story	~3000	0.78
12	4	0.4	350	10-story	~5000	0.79

Note: Values are approximate and read from the fitted curves.

The Figure 10 presents shear modulus degradation curves for (a) loose sand (Dr = 0.30), (b) medium-dense sand (Dr = 0.40), and (c) medium-dense sand (Dr = 0.50). For each density, three column lengths (150 mm, 250 mm, and 350 mm) are shown. The x-axis represents shear strain (γ, %), and the y-axis represents shear modulus (G, kPa). Medium-Dense sand (Dr = 0.50) exhibits higher initial shear modulus and slower degradation with increasing strain, indicating greater stiffness retention. Loose sand (Dr = 0.30) shows rapid modulus degradation, especially at shallow column lengths (150 mm), indicating stiffness loss and liquefaction susceptibility. Longer columns (350 mm) improve modulus retention across all densities.

4. Discussion

The data provide solid numbers to support how soil becomes more compact and clarify some of the finer points of how soil and structures interact.

The results are in good agreement with the well-established benchmark studies. Tokimatsu & Seed predicted volumetric strains of 2–4% for loose sand and cyclic stress ratios of 0.3–0.4, which agree well with our observed settlements (16–18 mm for a layer thickness of 500 mm, or 3.2–3.6%) [13]. Ishihara & Yoshimine [14] proposed that sands with $Dr > 0.45$ would show dilative behavior under cyclic loading; our results for $Dr = 0.50$ show (ru) always below 1.0 in most of the improved configurations, confirming this threshold experimentally. Sitar & Hausler, based on field case histories, suggested that improvement depth must be greater than about 70% of liquefiable thickness for reliable settlement control; our data (L = 350 mm = 70% of a 500 mm layer producing settlements < 2 mm, while L = 150 mm = 30% producing settlements > 16 mm) provide experimental confirmation of their field-based recommendation [15]. This observation applies to the conditions tested here: a 500 mm liquefiable layer, Dr = 0.30 to 0.50, a triangular column arrangement with a 18.2% replacement ratio, and the Kocaeli earthquake motion. It should not be generalized to other layer thicknesses, soil types, or seismic demands without further testing.

The difference in (ru) values between loose, medium-dense, and dense sands is controlled by their contractive or dilative behaviors under cyclic loading. Loose sand (Dr = 0.30, e = 0.776) is contractive: particles rearrange and collapse into voids during shaking, transferring stress from soil to pore water. Under undrained conditions, the water cannot escape quickly, so excess pore pressure builds up rapidly, leading to full liquefaction. If (ru) is close to or approximately one, water will flow to the surface, often in the form of sand boils.

It should be noted that the scatter in (ru) values between sensors reflects spatial variability in the model, not measurement error. Each transducer sits at a different location relative to the foundations and columns, so the local stress state and drainage conditions differ. This is consistent with observations from centrifuge and shaking-table studies [12,36]. The conclusions are based on the maximum (ru) value at each configuration to remain conservative.

Medium-Dense sand (Dr = 0.50, e = 0.711) is dilative: when sheared, tightly packed particles try to move apart, creating negative pore pressure (suction). The soil is stabilized by the increased effective stress due to the suction, which prevents (ru) from reaching 1.0. Even at positive pressure build-up, the decay is faster because of the smaller compressibility.

It is important to consider that the absence of suction measurements means we cannot fully explain the mechanism by which dense sand resists liquefaction. The measured (ru) values may be biased toward positive pressures for Dr = 0.50. In reality, dilative behavior in dense sand generates negative pore pressure (suction), which temporarily increases effective stress and helps prevent (ru) from reaching 1.0. Since the transducers cannot record negative pressures, the suction contribution is invisible in our data. This does not invalidate the observed trend—lower (ru) and settlement at higher (Dr), but it does mean the pore-pressure response of dense sand is only partially captured. The same limitation applies to medium-dense sand (Dr = 0.40) when it enters a dilative phase after initial contraction. Therefore, the (ru) values reported here should be viewed as positive-pressure indicators, not as a full effective-stress history.

The medium-dense sand (Dr = 0.40, e = 0.744) exhibits transitional behavior. Initial contraction leads to positive pressure, but dilation can happen after sufficient strain. This explains the wide (ru) range (0.64–1.0) and the column length and building load dependency. Loose sand has higher permeability, but pore pressure generation is faster

than dissipation in rapid cyclic loading. Thus, the primary mechanism by which densification improves liquefaction resistance is by altering the volumetric response from contractive to dilative, not by altering the permeability.

The medium-dense sand (Dr = 0.40) shows the widest range of the (ru) values, from 0.64 to 1.0. This reflects its transitional behavior between contractive loose sand and dilative dense sand. Based on the hysteresis loops in Figure 9, the 250 mm column (Test 11) produces the widest and most pinched loops, indicating significant cyclic softening and energy dissipation, while the 150 mm and 350 mm columns produce narrower loops. This suggests that at Dr = 0.40, the soil can exhibit either contractive or dilative behavior depending on the local drainage conditions, column length, and foundation load. The physical origin is that the sand fabric is in a transitional state: initial contraction generates positive pore pressure, but after sufficient strain, dilation can occur, producing suction and temporary strength recovery. The unstable performance comes from this competition between contraction and dilation, which is sensitive to small changes in density, confinement, and loading path. This transitional performance was obtained under the specific replacement ratio, column geometry, and 1999 Kocaeli earthquake input adopted in this study and should not be generalized to all sand deposits with Dr = 0.40.

Soil type (relative density) also directly and significantly affects the foundation settlement, as shown in Figure 7 and Table 8. The loose sand (Dr = 0.30, e = 0.776) experienced the largest settlements (up to 9 mm for the 150 mm columns in Test 4). This is because of the contractive nature of loose sand. Cyclic shaking causes particles to rearrange themselves into a denser packing, which reduces the void ratio and results in expulsion of water. This collapse is expressed in the volumetric strain (settlement/layer thickness = 9 mm/500 mm ≈ 1.8%).

Conversely, medium-dense sand (Dr = 0.50, e = 0.711) consistently exhibited minimal settlement, typically ranging from −0.4 mm in test 3 to −7 mm in test 9. This is attributed to its dilative behavior, where particle expansion under shear generates negative pore pressure, increasing effective stress and preventing volumetric collapse. This mechanism limits settlement even with elevated pore pressure ratios.

Medium-dense sand (Dr = 0.40, e = 0.744) exhibits moderate settlement (−14 mm in test 11). Its transitional behavior, initially contractive but subsequently dilative, limits total settlement compared to looser states.

Settlement under cyclic loading is governed by volumetric response, not permeability. Contractive (loose) soils settle, whereas dilative (dense) soils resist deformation. Densification (Dr = 0.30 to 0.50) significantly reduces settlement, exemplified by a reduction from 9 mm in test 4 to −0.4 mm in test 7 in 150 mm columns.

The Cyclic Resistance Ratio (CRR) framework is consistent with the close-to-total reduction of pore pressure in medium-dense sand (Dr = 0.50) [9,37]. Increasing Dr increases the CRR by improving soil structure stability. Achieving a sufficient density shifts the soil's intrinsic CRR above the site-specific seismic demand, a direct performance-based design outcome because the Cyclic Stress Ratio (CSR) induced by the scaled Kocaeli motion was insufficient to cause significant pore pressure in the dense configuration.

It should also be noted that the mechanical properties of the cement–sand columns were not measured directly in this study. The expected 7-day UCS of 0.5–1.0 MPa is an empirical estimate based on published correlations for similar cement contents and w/c ratios. The column stiffness and strength discussed in this section should therefore be regarded as approximate, and the interpretation focuses on relative performance rather than absolute column capacity.

There are significant effects of the sharp decline in settlement. Large, sharp settlements in loose sand are indicative of flow deformation after shear strength loss [38]. The minimal settlements in dense sand attest to the fact that volumetric collapse is avoided

by maintaining effective stress. This behavior is consistent with established approaches for estimating liquefaction-induced settlement. Ishihara & Yoshimine related post-liquefaction volumetric strain to relative density and the factor of safety against liquefaction, while Zeghal & Elgamal [30] related volumetric strain to cyclic stress ratio and soil resistance [14]. More recently, Bray & Macedo [39] developed a simplified procedure for estimating liquefaction-induced building settlement that also accounts for shear-induced deformation and soil–structure interaction.

The term "insignificant" was avoided because no formal performance criterion was used. For context, 7 mm at model scale corresponds to 140 mm at prototype scale, which may exceed typical serviceability limits for a 15-story building. The best performance was achieved with L = 250–350 mm, where settlements were below 2 mm (40 mm prototype), but even these values require evaluation against project-specific criteria.

One important caveat is that the experiments used a homogeneous sand deposit. Real alluvial and coastal sites are often stratified, with silt or clay seams, gravel lenses, or variable density. These features can block or channel drainage, change confinement, and create local zones of pore-pressure build-up that a uniform model cannot reproduce. The trends we observed—higher (*Dr*) leads to lower (*ru*) and less settlement—should still hold in layered ground, but the absolute values and the rate of dissipation may differ. So, the results should be applied to stratified sites only after site-specific evaluation.

The dynamic properties of soil can be understood through the evolution of damping and shear modulus. The observed period elongation and high damping, which lower transmitted high-frequency accelerations at the expense of bearing capacity, are explained by the severe degradation of G in loose sand. This demonstrates the dual nature of liquefaction, which can both cause geotechnical failure and offer seismic isolation [29]. By maintaining a high G, densification ensures a predictable foundation response and avoids this risky strength-loss isolation.

The scatter in the shear modulus data reflects the inherent variability of physical model tests, including local density variations, sensor placement, and integration errors. The fitted degradation curves carry an estimated uncertainty of ±15% in G, as noted earlier, and the R^2 values range from 0.72 to 0.81. Despite this scatter, the relative increase in secant modulus with density is clear for the lighter foundation but less consistent for the heavier one.

Medium-dense sand (Dr = 0.40) is a key point. It didn't completely liquefy but showed partial pore pressure and some settlement. This suggests a non-linear pattern: small density increases below a certain point don't help much, but going past that point (like to Dr = 0.50) greatly improves performance. For the Kocaeli earthquake, a density of 0.40 might not be safe enough for important structures, while 0.50 offers a good safety buffer.

Structure weight mattered. The taller building (15 stories) caused slightly greater pore pressure and settlement due to higher static shear stress and bearing pressure. This agrees with Bertalot et al., who said bearing pressure is important for settlement [40]. Our data indicate that making the soil denser separates settlement from structure weight; in dense soil, settlement differences between structures were small.

The effect of superstructure load was examined by comparing the 10-story (30 kg) and 15-story (45 kg) models. The 15-story model imposed a higher bearing pressure. In several tests, the heavier building caused slightly greater pore pressure and settlement. For example, in Test 6 (Dr = 0.3, L = 350 mm), the (ru) below the 15-story building was 0.34, while below the 10-story building it was 0.57; the lighter building showed higher (ru) in that case. In other tests, the heavier building showed higher (ru). The pattern is not consistent, which suggests that foundation load interacts with column length and soil density in a complex way. In dense soil, the difference between the two buildings was

small, suggesting that densification reduces the sensitivity of settlement to structure weight.

This research links component experiments to real-world performance. Though repeated load tests on Firuzkuh sand could also show greater resistance as relative density increases, our combined model accounts for how the system works: stress changes under foundations, actual drainage conditions, and how soil weakening and structural behavior affect each other. This provides total verification for computer models of enhanced ground.

Limitations

Several limitations should be considered when interpreting the findings of this study. First, the experimental program assumed a homogeneous sand profile, whereas natural soil deposits are often stratified and heterogeneous. Variations in permeability and layering can influence drainage conditions, confinement, and consequently the soil response under seismic loading.

Second, the seismic input was based solely on the 1999 Kocaeli earthquake, characterized by its specific frequency content, duration, and amplitude. Other major earthquakes, such as the 1995 Kobe, 2011 Tohoku, and 2023 Kahramanmaraş events, exhibit different ground motion characteristics, including variations in magnitude, peak ground acceleration, and frequency spectra. These differences may affect the magnitude of pore pressure generation and settlement. Although general trends—such as reduced pore pressure ratio and settlement with increasing relative density—are expected to remain consistent, the exact numerical results may vary under different seismic conditions.

Third, the study utilized Firuzkuh sand, a clean and uniformly graded sand (*SP*). Therefore, the findings may not be directly applicable to soils containing fines, such as silty or clayey sands, gravelly materials, or highly plastic soils. Such materials require site-specific evaluation due to their distinct mechanical behavior.

Fourth, the pore pressure sensors used (0–100 kPa range) were limited to measuring positive pore pressures. As a result, negative pore pressures (suction), which may develop in dense sands exhibiting dilative behavior, could not be captured.

Fifth, the 1 g shaking table tests cannot fully satisfy stress similarity. The stress state, strain rate, and drainage path length in the model differ from prototype conditions. Absolute values such as settlement should not be directly extrapolated to full scale without correction. Relative comparisons between tests remain valid.

Sixth, the columns were constructed by in-situ mixing of sand with cement, which is classified as a deep mixing method but shares characteristics with deep replacement. This differs from field deep mixing, where the binder is mixed with the native soil. The column-soil interface is sharper and the cement distribution more uniform than in the field, which may affect interface friction and stiffness. The columns represent the overall function of deep mixing elements, not the exact construction process.

Seventh, the shear stress-strain loops were derived from double integration of acceleration records without independent validation against cyclic triaxial or simple shear tests on the same sand. Estimated uncertainties are ±15% for shear modulus and ±20% for damping ratio.

Eighth, the cement-sand column material was not tested for unconfined compressive strength, modulus, or stress-strain behavior. Based on the mix design, the expected 7-day UCS is 0.5–1.0 MPa, which is lower than typical field deep-mixing columns. This should be considered when extrapolating the results to field-scale applications.

Ninth, the absence of an experimental unimproved reference test under the Kocaeli motion is acknowledged.

Tenth, the shear modulus degradation curves were fitted using the Hardin–Drnevich model with R^2 values between 0.72 and 0.81. The scatter in the data and the uncertainty in the fitting procedure should be considered when using these curves for design.

Eleventh, no formal performance criterion was adopted to define acceptable settlement. The measured settlements, including the 7 mm value for the 15-story building at Dr = 0.50 with a short column, should be evaluated against project-specific serviceability limits in future work. At prototype scale, 7 mm model settlement corresponds to 140 mm, which may be significant for tall buildings.

Twelfth, the applicability of the present results to other soil types is limited. The experiments were conducted using Firuzkuh sand (Code 161), a clean, uniformly graded sand classified as SP. This controlled material was selected to isolate the effect of relative density, but natural deposits may contain varying amounts of silt, clay, or gravel. Such differences can modify particle fabric, drainage characteristics, compressibility, cyclic resistance, and pore-pressure generation. Therefore, the quantitative values of R_u settlement and dynamic soil properties obtained in this study should not be directly transferred to silty sands, clayey sands, gravelly soils, or soils with significant fines content.

Finally, the seismic input was limited to the N–S component of the 1999 Kocaeli earthquake recorded at Yarımca. Earthquakes with different magnitude, duration, amplitude, frequency content, and cyclic characteristics may produce different responses.

5. Conclusions

Soil liquefaction poses a significant threat to buildings in earthquake-prone regions, leading to a reduction in bearing capacity, foundation settlement, and structural damage. In this study, the effects of relative density (Dr = 0.30, 0.40, and 0.50) on the liquefaction resistance of Firuzkuh sand under seismic loading simulating the Kocaeli earthquake of 1999 were experimentally investigated. The study was conducted on a 1-g shaking table using 10- and 15-story scaled building models. Pore pressure ratio (ru), foundation settlement, shear modulus, and damping ratio were measured.

The results show that increasing the relative density from 0.30 to 0.40 significantly improves the behavior of soil during shaking. In particular, peak pore pressure ratios reduced from 1.0 in loose sand to 0.64 in medium-dense sand (for similar column lengths); foundation settlements reduced from over 9 mm in loose sand to zero in the best-performing configurations (shorter columns), though shorter columns at Dr = 0.50 still produced settlements −6.5 mm; shear modulus increased by a factor of 3 to 4; and damping ratio reduced significantly. Medium-dense sand (Dr = 0.50) substantially reduced the extent and severity of liquefaction, but it did not prevent liquefaction everywhere; some sensors in the middle zone between buildings still recorded (ru) values above 1.0. The 70% column length observation applies specifically to the 500 mm liquefiable layer and the conditions tested here. It should not be generalized to other layer thicknesses, soil types, or seismic demands without further testing. The medium-dense sand (Dr = 0.40) provided only limited protection, with residual pore pressure and moderate settlement, indicating a non-linear performance pattern: little benefit from small density increases below a threshold, but significant safety improvements beyond it.

If you're working on engineering projects in places prone to earthquakes, like Turkey's Marmara region, it's recommended that clean sand have a relative density of at least 0.50. This threshold was derived from tests using the Kocaeli earthquake motion only. It should not be applied directly to other earthquakes with different magnitude, frequency content, or duration without site-specific evaluation. This is especially important when you're anticipating strong, long-lasting shaking, similar to what happened during the

Kocaeli earthquake. Our experiments really back up this idea, giving us a solid foundation for designing ground improvements that can hold up well.

It is important to mention that these results are from the 1999 Kocaeli ground motion and Firuzkuh sand. Although the general trends state that a higher Dr decreases the risk of liquefaction and are expected to hold for other clean sands, the exact quantitative thresholds may differ for soils with high fines content, gravelly soils, or plastic silts and clays.

Recommendations

In earthquake-prone areas such as the Marmara region of Turkey, for clean sands (SP classification, fines content < 10%) under shallow foundations, it is recommended to compact the soil to a relative density of no less than 0.50 when strong, long-duration shaking similar to the 1999 Kocaeli earthquake is anticipated. This threshold was derived from tests using the Kocaeli earthquake motion only. It should not be applied directly to other earthquakes with different magnitude, frequency content, or duration without site-specific evaluation. This recommendation applies specifically to clean sands; soils with high fines content, gravelly soils, or plastic silts and clays require site-specific evaluation.

Future research is suggested to:

1. Validate the findings at field scale in Kocaeli or similar liquefiable regions
2. Repeat the experiments with other recorded ground motions, including the 1995 Kobe, 1995 Northridge, 2011 Tohoku and 2023 Kahramanmaraş earthquakes, using records from AFAD and other Turkish strong-motion databases.
3. Test other soil types, including silty sands, clayey sands, gravelly soils, and soils with significant fines content, to evaluate how far the observed trends apply.
4. Study hybrid ground improvement techniques, such as densification combined with vertical drains, or sand–cement columns with gravel blankets, to accelerate pore-pressure dissipation.
5. Carry out economic and sustainability comparisons of different densification and deep replacement techniques.
6. Develop regional liquefaction risk maps for seismically active coastal zones using the experimental G–γ, damping, and ru relationships from this study in numerical models.
7. Validate the shear stress–strain relationships derived from acceleration records with independent element-scale cyclic triaxial or simple shear tests on the same sand.
8. Measure the unconfined compressive strength, modulus, and stress–strain behavior of the cement–sand column material in future studies.
9. Use pressure transducers that can measure both positive and negative pore pressures (e.g., differential pressure transducers or tensiometers) in future shaking-table tests, especially for dense sands, to capture suction.
10. Include unimproved reference tests under the same input motion to quantify the absolute improvement factor of the columns.
11. Include layered soil profiles to examine how stratification affects the density–liquefaction relationship.

Author Contributions: S.M.: Conceptualization (equal), Methodology (equal), Investigation (lead), Formal analysis (lead), Data curation (lead), Writing—original draft (lead), Visualization (lead). H.B.: Conceptualization (equal), Methodology (equal), Validation (lead), Resources (lead), Supervision (lead), Project administration (lead), Writing—review and editing (lead), Funding acquisition (lead). All authors have read and agreed to the published version of the manuscript.

Funding: This research received no external funding.

Institutional Review Board Statement: Not applicable.

Informed Consent Statement: Not applicable.

Data Availability Statement: The datasets generated and analyzed during the current study are not publicly available due to proprietary restrictions but are available from the corresponding author on reasonable request.

Conflicts of Interest: The authors declare no conflicts of interest.

References

1. Sancio, R.B.; Bray, J.D.; Stewart, J.P.; Youd, T.L.; Durgunoğlu, H.T.; Önalp, A.; Seed, R.B.; Christensen, C.; Baturay, M.B.; Karadayılar, T. Correlation between ground failure and soil conditions in Adapazari, Turkey. *Soil Dyn. Earthq. Eng.* **2002**, *22*, 1093–1102. https://doi.org/10.1016/S0267-7261(02)00135-5.
2. Cetin, K.O.; Youd, T.L.; Seed, R.B.; Bray, J.D.; Sancio, R.; Lettis, W.; Yilmaz, M.T.; Durgunoglu, H.T. Liquefaction-induced ground deformations at Hotel Sapanca during Kocaeli (Izmit), Turkey earthquake. *Soil Dyn. Earthq. Eng*. **2002**, *22*, 1083–1092. https://doi.org/10.1016/S0267-7261(02)00134-3.
3. Youd, T.L.; Idriss, I.M.; Andrus, R.D.; Arango, I.; Castro, G.; Christian, J.T.; Dobry, R.; Finn, W.D.L.; Harder, L.F., Jr.; Hynes, M.E.; et al. Liquefaction Resistance of Soils: Summary Report from the 1996 NCEER and 1998 NCEER/NSF Workshops on Evaluation of Liquefaction Resistance of Soils. *J. Geotech. Geoenviron. Eng.* **2001**, *127*, 817–833. https://doi.org/10.1061/(ASCE)1090-0241(2001)127:10(817).
4. Idriss, I.M.; Boulanger, R.W. *Soil Liquefaction During Earthquakes*; Earthquake Engineering Research Institute: Oakland, CA, USA, 2008.
5. Towhata, I. *Geotechnical Earthquake Engineering*; Springer: Berlin/Heidelberg, Germany, 2008.
6. Kirsch, K.; Kirsch, F. *Ground Improvement by Deep Vibratory Methods*, 2nd ed.; CRC Press: Boca Raton, FL, USA, 2016.
7. Ishihara, K. *Soil Behaviour in Earthquake Geotechnics*; Clarendon Press: Oxford, UK, 1996.
8. Seed, H.B.; Tokimatsu, K.; Harder, L.F.; Chung, R.M. Influence of SPT Procedures in Soil Liquefaction Resistance Evaluations. *J. Geotech. Eng*. **1985**, *111*, 1425–1445. https://doi.org/10.1061/(ASCE)0733-9410(1985)111:12(1425).
9. Seed, H.B.; Idriss, I.M. *Ground Motions and Soil Liquefaction During Earthquakes*; Earthquake Engineering Research Institute: Oakland, CA, USA, 1982.
10. Iai, S. Similitude for Shaking Table Tests on Soil-Structure-Fluid Model in 1g Gravitational Field. *Soils Found*. **1989**, *29*, 105–118. https://doi.org/10.3208/sandf1972.29.105.
11. Liu, L.; Dobry, R. Seismic response of shallow foundation on liquefiable sand. *J. Geotech. Geoenviron. Eng*. **1997**, *123*, 557–567. https://doi.org/10.1061/(ASCE)1090-0241(1997)123:6(557).
12. Dashti, S.; Bray Jonathan, D.; Pestana Juan, M.; Riemer, M.; Wilson, D. Mechanisms of Seismically Induced Settlement of Buildings with Shallow Foundations on Liquefiable Soil. *J. Geotech. Geoenviron. Eng.* **2010**, *136*, 151–164. https://doi.org/10.1061/(ASCE)GT.1943-5606.0000179.
13. Tokimatsu, K.; Seed, H.B. Evaluation of Settlements in Sands Due to Earthquake Shaking. *J. Geotech. Eng*. **1987**, *113*, 861–878. https://doi.org/10.1061/(ASCE)0733-9410(1987)113:8(861).
14. Ishihara, K.; Yoshimine, M. Evaluation of settlements in sand deposits following liquefaction during earthquakes. *Soils Found.* **1992**, *32*, 173–188. https://doi.org/10.3208/sandf1972.32.173.
15. Sitar, N.; Hausler, E. Influence of Ground Improvement on Liquefaction Induced Settlement: Observations from Case Histories and Centrifuge Experiments. *Int. J. Geo-Eng.* **2012**, *4*, 5–15.
16. Ueng, T.-S.; Wang, M.-H.; Chen, M.-H.; Chen, C.-H.; Peng, L.-H. A Large Biaxial Shear Box for Shaking Table Test on Saturated Sand. *Geotech. Test. J.* **2006**, *29*, 1–8. https://doi.org/10.1520/gtj12649.
17. Asadzadeh, G.; Bahadori, H. Investigating the dynamic response of deep mixing columns and gravel columns in liquefiable layer with different thickness. *Amirkabir J. Civ. Eng.* **2023**, *55*, 619–640. https://doi.org/10.22060/ceej.2023.21772.7821.
18. Prasad, S.K.; Towhata, I.; Chandradhara, G.P.; Nanjundaswamy, P. Shaking Table Tests in Earthquake Geotechnical Engineering. *Curr. Sci.* **2004**, *87*, 1398–1404.
19. Farahmand, K.; Lashkari, A.; Ghalandarzadeh, A. Firoozkuh Sand: Introduction of a Benchmark for Geomechanical Studies. *Iran. J. Sci. Technol. Trans. Civ. Eng.* **2016**, *40*, 133–148. https://doi.org/10.1007/s40996-016-0009-0.

20. *ASTM D854-23*; Standard Test Methods for Specific Gravity of Soil Solids by Water Pycnometer. ASTM: West Conshohocken, PA, USA, 2023. https://doi.org/10.1520/D0854-23.
21. *ASTM D4253-16*; Standard Test Methods for Maximum Index Density and Unit Weight of Soils Using a Vibratory Table. ASTM: West Conshohocken, PA, USA, 2016. https://doi.org/10.1520/D4253-16.
22. *ASTM D4254-14*; Standard Test Methods for Minimum Index Density and Unit Weight of Soils and Calculation of Relative Density. ASTM: West Conshohocken, PA, USA, 2014. https://doi.org/10.1520/D4254-14.
23. *ASTM D422-63(2007)*; Standard Test Method for Particle-Size Analysis of Soils (Withdrawn 2016). ASTM: West Conshohocken, PA, USA, 2007. https://doi.org/10.1520/D0422-63R07.
24. *ASTM D6913/D6913M-17(2025)*; Standard Test Methods for Particle-Size Distribution (Gradation) of Soils Using Sieve Analysis. ASTM: West Conshohocken, PA, USA, 2025. https://doi.org/10.1520/D6913_D6913M-17R25.
25. Das, B.M.; Sivakugan, N. *Principles of Foundation Engineering*; Cengage Learning: Boston, MA, USA, 2018.
26. Bruce, D.A. Practitioner's guide to the deep mixing method. *Proc. Inst. Civ. Eng.-Ground Improv.* **2001**, *5*, 95–100. https://doi.org/10.1680/grim.2001.5.3.95.
27. Kitazume, M.; Terashi, M. *The Deep Mixing Method*; CRC Press: Leiden, The Netherlands, 2013.
28. Porbaha, A. State of the art in deep mixing technology: Part I. Basic concepts and overview. *Proc. Inst. Civ. Eng.-Ground Improv.* **1998**, *2*, 81–92. https://doi.org/10.1680/gi.1998.020204.
29. Karamitros, D.K.; Bouckovalas, G.D.; Chaloulos, Y.K. Insight into the Seismic Liquefaction Performance of Shallow Foundations. *J. Geotech. Geoenviron. Eng.* **2013**, *139*, 599–607. https://doi.org/10.1061/(ASCE)GT.1943-5606.0000797.
30. Zeghal, M.; Elgamal, A.-W. Analysis of Site Liquefaction Using Earthquake Records. *J. Geotech. Eng.* **1994**, *120*, 996–1017. https://doi.org/10.1061/(ASCE)0733-9410(1994)120:6(996).
31. Elgamal, A.-W.; Zeghal, M.; Parra, E. Liquefaction of Reclaimed Island in Kobe, Japan. *J. Geotech. Eng.* **1996**, *122*, 39–49. https://doi.org/10.1061/(ASCE)0733-9410(1996)122:1(39).
32. Kramer, S.L.; Stewart, J.P. *Geotechnical Earthquake Engineering*; CRC Press: Boca Raton, FL, USA, 2024.
33. Hardin, B.O.; Drnevich, V.P. Shear Modulus and Damping in Soils: Design Equations and Curves. *J. Soil Mech. Found. Div.* **1972**, *98*, 667–692. https://doi.org/10.1061/JSFEAQ.0001760.
34. PEER. *PEER Ground Motion Database (NGA-West2)*; PEER: New York, NY, USA, 2013.
35. Seed, H.B.; Idriss, I.M. Simplified procedure for evaluating soil liquefaction potential. *J. Soil Mech. Found. Div.* **1971**, *97*, 1249–1273. https://doi.org/10.1061/JSFEAQ.0001662.
36. Jafarian, Y.; Mehrzad, B.; Lee, C.J.; Haddad, A.H. Centrifuge modeling of seismic foundation-soil-foundation interaction on liquefiable sand. *Soil Dyn. Earthq. Eng.* **2017**, *97*, 184–204. https://doi.org/10.1016/j.soildyn.2017.03.019.
37. Youd, T.L.; Hansen Corbett, M.; Bartlett Steven, F. Revised Multilinear Regression Equations for Prediction of Lateral Spread Displacement. *J. Geotech. Geoenviron. Eng.* **2002**, *128*, 1007–1017. https://doi.org/10.1061/(ASCE)1090-0241(2002)128:12(1007).
38. Ishihara, K. Liquefaction and flow failure during earthquakes. *Géotechnique* **1993**, *43*, 351–451. https://doi.org/10.1680/geot.1993.43.3.351.
39. Bray, J.D.; Macedo, J. 6th Ishihara lecture: Simplified procedure for estimating liquefaction-induced building settlement. *Soil Dyn. Earthq. Eng.* **2017**, *102*, 215–231. https://doi.org/10.1016/j.soildyn.2017.08.026.
40. Bertalot, D.; Brennan, A.J.; Villalobos, F.A. Influence of bearing pressure on liquefaction-induced settlement of shallow foundations. *Géotechnique* **2013**, *63*, 391–399. https://doi.org/10.1680/geot.11.P.040.

Disclaimer/Publisher's Note: The statements, opinions and data contained in all publications are solely those of the individual author(s) and contributor(s) and not of MDPI and/or the editor(s). MDPI and/or the editor(s) disclaim responsibility for any injury to people or property resulting from any ideas, methods, instructions or products referred to in the content.